The Meteoritical Society

Meteoritics & Planetary Science 44, Nr 7, 1061–1086 (2009)
Abstract available online at http://meteoritics.org

Cosmogenic nuclides in stony meteorites revisited

Ingo LEYA[1*], and Jozef MASARIK[2]

[1]Space Sciences and Planetology, University of Bern, Bern 3012, Switzerland
[2]Department of Nuclear Physics and Biophysics, Faculty of Mathematics, Physics and Informatics, Commenius University Bratislava, Slovakia
[*]Corresponding author. E-mail: ingo.leya@space.unibe.ch

(Received 05 August 2008; revision accepted 12 April 2009)

Abstract–We present new model calculations for depth and size dependent cosmogenic production rates in ordinary and carbonaceous chondrites by galactic cosmic rays. This model, essentially that of Leya et al. (2000a), folds together particle spectra and cross sections for the relevant nuclear reactions, but has been significantly improved due to major improvements in the neutron cross section database and better Monte Carlo modeling of the primary and the secondary particle spectra. The data presented here replace (and extend) the results of our earlier model predictions. Here we give for ordinary and carbonaceous chondrites elemental production rates for the cosmogenic radionuclides ^{10}Be, ^{14}C, ^{26}Al, ^{36}Cl, ^{41}Ca, ^{53}Mn, ^{60}Fe, and ^{129}I as well as for the noble gas isotopes ^{3}He, ^{4}He, ^{20}Ne, ^{21}Ne, ^{22}Ne, ^{36}Ar, and ^{38}Ar. Using the new data and expressing size and depth scales to the unit [g/cm^2], we are able to demonstrate that the matrix effect for both chondrite types is negligible for all target product combinations, except for those which are dominated by thermal or very low energy neutron reactions. Based on the new model predictions, we present a variety of elemental and isotopic production rate ratios allowing for a reliable determination of preatmospheric sizes, shielding depths, cosmic-ray exposure ages, and diffusive losses.

INTRODUCTION

Cosmic-ray-produced nuclides provide important information about irradiation histories of meteorites, in particular preatmospheric radii, sample locations, exposure ages, terrestrial residence times, and whether the meteoroids experienced a complex exposure. Combining such data for many meteoroids enables one to obtain crucial data for parent body processes, for example major collisional events, surface survival times, and gardening rates on the surface of an asteroid as well as regolith exposure histories. Information about the orbital dynamic of small bodies in the solar system becomes also accessible. For example, most H chondrites have cosmic-ray exposure ages of ~7 Ma, indicating that meteoroid production was not (and probably is not) a continuous processes, at least not for H chondrites, but is dominated by a few catastrophic collisions. For a proper interpretation of cosmogenic nuclide abundances, the depth-, size-, and matrix-dependency of the production rates have to be known. During the last few decades, a variety of models have been proposed (e.g., Signer and Nier 1960; Arnold et al. 1961; Reedy and Arnold 1972; Graf et al. 1990a; Michel et al. 1991; Masarik and Reedy 1994; Leya et al. 2000a). For recent reviews see Wieler (2002), Herzog (2005), and Eugster et al. (2006).

In Leya et al. (2000a), we published a comprehensive data set for depth- and size-dependent production rates of cosmogenic nuclides by galactic cosmic-ray particles (GCR) for ordinary chondrites with radii from 5 cm to 120 cm. In that study, we used a purely physical model with only one free parameter, the integral number of galactic cosmic-ray particles. The model was based on the best available knowledge of the primary and secondary particle spectra and the excitation functions for the relevant nuclear reactions. Since then our modeling of the differential particle spectra as well as our knowledge of the relevant nuclear reactions, especially for neutron induced reactions, has significantly been improved. For example, the neutron excitation functions used in our earlier approach were derived from five thick target simulation experiments by an energy dependent least squares adjustment procedure (e.g., Leya et al. 2000b). However, such an adjustment suffers from the fact that the number of experimental data, i.e., measured elemental production rates in the thick target experiments, is significantly less than the number of neutron cross sections needed for proper modeling. To circumvent this problem, the adjustment procedure requires a guess function as an input for each neutron excitation function to be determined. In our earlier approach the guess functions were calculated using the

AREL- (M. Blann 1994, personal communication with Rolf Michel) and the ALICE-IPPE code (Shubin et al. 1995). However, both models suffer from the fact that they often failed to accurately predict the threshold energies. This shortcoming resulted, in some cases, in unphysical structures in the determined neutron excitation functions. However, in the last few years, some of the nuclear model codes have significantly been improved, and one of the best codes currently available is TALYS (Koning et al. 2005). Based on the improved guess functions, we are now able to determine neutron excitation functions which are more reliable than the earlier ones. In addition to the better quality of the neutron cross sections, we also improved the differential particle spectra. While in our earlier approach the spectra of primary and secondary particles were calculated using the HET- (Armstrong and Chandler 1972) and MORSE-codes (Emmett 1975) within the HERMES code system (Cloth et al. 1988) in the current project we use the LAHET-code system (Masarik and Reedy 1994 and references therein).

Here we present new model predictions for the production of the cosmogenic radionuclides ^{10}Be, ^{14}C, ^{26}Al, ^{36}Cl, ^{41}Ca, ^{53}Mn, ^{60}Fe, and ^{129}I as well as of the noble gas isotopes ^{3}He, ^{4}He, ^{20}Ne, ^{21}Ne, ^{22}Ne, ^{36}Ar, and ^{38}Ar in ordinary chondrites with radii between 10 cm and 500 cm. In addition and for the first time we present a comprehensive data set for the production rates—of the same set of cosmogenic nuclides—in carbonaceous chondrites with radii between 10 cm and 500 cm. The latter might differ from the former due to the matrix effect, i.e., the dependence of the production rates on the chemical composition of the meteoroid, which we also discuss in some detail. In this study we focus on radionuclides and He, Ne, and Ar isotopes. The model predictions for Kr and Xe isotopes will be given elsewhere. In addition to the depth, size, and matrix dependency of the elemental production rates, we present a variety of cosmogenic nuclide correlations, which might be useful for the determination of preatmospheric radii, shielding depths, exposure ages, and terrestrial residence times. For the latter discussion we focus on ordinary chondrites because i) they make up the majority of all (known) meteorites and ii) a detailed discussion of carbonaceous chondrites would make this paper too long. However, such correlations can easily be calculated by the reader. We therefore give the elemental production rates for ordinary chondrites ("OC") and carbonaceous chondrites ("CC") as Excel files on our website http://www. noblegas.unibe.ch or upon request from the corresponding author. Doing so we prepared four Excel files: "Prts_OC_ Radionuclides.xls" and "Prts_OC_NobleGases. xls" for the elemental production rates of cosmogenic radionuclides and noble gases, respectively, in ordinary chondrites and "Prts_CC_Radionuclides.xls" and "Prts_CC_NobleGases. xls" for the respective data for carbonaceous chondrites.

THE PHYSICAL MODEL

The physical model is essentially the same as the one used earlier by us (Leya et al. 2000a, 2001a; Ammon et al. 2008a; see also Michel et al. 1991). Briefly, the production rate P_j [atoms/(g × s)] of a cosmogenic nuclide j is calculated via:

$$P_j(R, d, M) = \sum_{i=1}^{N} c_i \frac{N_A}{A_i} \sum_{k=1}^{3} \int_0^{\infty} \sigma_{j,i,k}(E) \times J_k(E, R, d, M) dE \quad (1)$$

where N_A is Avogadro's number, A_i is the mass number of the target element i, c_i is the abundance of i [g/g], and k is an index for the reaction particle type (protons and neutrons). The excitation function for the production of nuclide j from target element i by reactions induced by particle type k is $\sigma_{j,i,k}$ [cm^2] and J_k [1/(cm^2 × s × MeV)] is the differential flux density of particles of type k. The radius of the meteoroid, which is assumed to be spherical, is R, d is the shielding depth of the sample, and E and M are the energy of the reacting particles and the solar modulation parameter, respectively. The solar modulation parameter M [MeV] is the energy lost by a GCR particle when it enters the solar system and approaches a given distance from the Sun. The current version of model calculations—as well as all earlier versions—explicitly takes into account only proton and neutron induced reactions. Primary and secondary galactic α-particles are considered in an approximate way, because the particle spectra and cross sections needed for accurate modeling are not yet available. For the approximation we assume that an incoming α-particle breaks up into four nucleons in the first inelastic collision. We further assume that these alpha-derived nucleons, two protons and two neutrons each containing ~25% of the original energy, have an energy distribution similar to that of the primary galactic protons. Since GCRs consist of 87% protons and 12% α-particles, the contribution from α-particles to the total production rates can be approximated by multiplying the production rates obtained for protons and neutrons with a factor of 1.55. We do not expect this approximation to be strictly valid for the production of ^{4}He, and we also expect some deviations for nuclides produced by low energy particles, e.g., ^{53}Mn from Fe. Every α-particle reacting directly and not breaking up produces cosmogenic nuclides but the number of secondary particles produced in this reaction is expected to be much smaller than the number of secondary particles which would have been produced by 2 protons and 2 neutrons, i.e., after the ^{4}He breakup. Consequently, every ^{4}He reacting directly reduces the (assumed) secondary particles fluxes and therefore reduces the production rates for such cosmogenic nuclides that are produced dominantly by low energy projectiles. We will discuss the shortcomings of the α-approximation in more detail below.

Cross Sections

For each cosmogenic nuclide, the model requires complete excitation functions for all relevant nuclear reactions. The new model calculations are based only on proton and neutron induced reactions, because the particle spectra of primary and secondary α-particles are not yet accurate enough (e.g., Boudard et al. 2002), and the cross section database for α-induced reactions is far from sufficient. For proton induced reactions we use essentially the same cross section database as in our earlier studies (Leya et al. 2000a, 2001a). In addition, for the production of ^{10}Be from C we use the cross sections given by Kim et al. (2002). For ^{41}Ca all cross sections are now normalized to the AMS standard IRMM4 (e.g., Schnabel et al. 1998), and for the production of ^{53}Mn we take into account the recent changes in the AMS standard and in the decay constant. These make the cross sections and consequently the modeled production rates higher by ~29% (Merchel, personal communication). Some of the consequences of these changes are discussed below. For the production of ^{3,4}He, ^{21,22}Ne, and ^{36,38}Ar from Fe and Ni we use the cross section database published recently by Ammon et al. (2008b). However, for some target product combinations the experimental database is still limited and reported measurements often disagree. For this reason, we had to extend and/or interpolate the excitation functions using nuclear model codes. Doing so we used the TALYS code (Koning et al. 2005), a computer code system for the prediction of nuclear reactions in the energy range 1 keV up to 200 MeV for target nuclides of mass 12 and heavier (Duijvestijn and Koning 2006). Broeders et al. (2006) demonstrated in a systematic study of different nuclear model codes that the TALYS code is, at least for proton induced reactions in the energy range up to 150 MeV and in the mass range below 150, one of the best codes currently available.

For neutron induced reactions the situation is less than ideal since there is only a limited number of cross section measurements (e.g., Reedy et al. 1979; Lavielle et al. 1990; Nakamura et al. 1991, 1992). The neutron cross section database used here, as well as in our recent study of iron meteorites (cf. Ammon et al. 2008a), is an improved version of the one used earlier by Leya et al. (2000a, 2000b, 2001a). Briefly, the neutron excitation functions are extracted from production rates obtained in five thick target simulation experiments (e.g., Michel et al. 1985, 1989, 1993; Lüpke 1993; Leya et al. 2000b). We start with a priori neutron excitation functions as guess functions and derive the a posteriori neutron cross sections, which are then used for modeling using an energy dependent least squares adjustment procedure. For more details see Leya and Michel (1998) and Leya et al. (2000b). The major improvement of the current neutron cross section database, compared to the earlier one (Leya et al. 2000a, 2000b, 2001a), is that in the current version the guess functions have been calculated using the TALYS code (Koning et al. 2005). This code is able not only to predict cross sections within (mostly) a factor of about 2, but also to describe reaction thresholds reliably. In our earlier study we had to calculate the guess functions using the AREL (Blann 1994, personal communication with R. Michel) and/or ALIPPE-IPPE code (Shubin et al. 1995), which usually failed describing (proton-induced) cross sections by about one order of magnitude (or more) and which very often failed to accurately predict threshold energies. As expected, using reliable guess functions as input data, the deconvolution procedure works much more reliably and therefore the a posteriori neutron cross sections are of much better quality than in our earlier study. To summarize, the major improvement of the current version of model calculations compared to our earlier studies (Leya et al. 2000b, 2001a) is due to the improvement of the neutron cross section database, made possible due to better input data used for the deconvolution procedure. A detailed discussion of the new neutron database will be given elsewhere.

By way of example, in Fig. 1 we show the excitation functions for the proton and neutron induced production of ^{10}Be from O and ^{26}Al from Al. As already discussed earlier (Leya and Michel 1998; Leya et al. 2000b) the figure demonstrates that the often used assumption of equal cross sections for proton- and neutron-induced reactions is generally not valid and, if nevertheless used, leads to erroneous production rates. For example, assuming equal cross sections for the proton- and neutron-induced production of ^{10}Be from O results in production rates about factor of 2–3 lower than the ones modeled using experimental proton cross sections and a posteriori neutron excitation functions.

Spectra of Primary and Secondary Particles—Shapes and Normalizations

The depth- and size-dependent spectra of primary and secondary particles are calculated using the LAHET code system (cf. Masarik and Reedy 1994 and references therein). With LAHET we simulated for L and CI chondrites with radii of 10, 20, 25, 30, 35, 40, 50, 65, 85, 100, 120, 150, 200, 300, and 500 cm the intra- and internuclear cascades of primary and secondary particles using Monte-Carlo techniques assuming a solar modulation parameter M = 550 MeV. The spectra calculated for L chondrites are also valid for most other chondrite classes, because the differences in spectral shapes and flux densities due to different chemical compositions, i.e., the matrix effects, are small for most of the target product combinations considered here (Lange 1994; Masarik and Reedy 1994). This is not true if we consider extreme variations in the chemical composition. For example Masarik and Reedy (1994) reported sizeable effects between ordinary chondrites and, e.g., mesosiderites. In addition, it is also not true for reactions induced by thermal neutrons, because their flux densities do vary with meteorite type, even between H

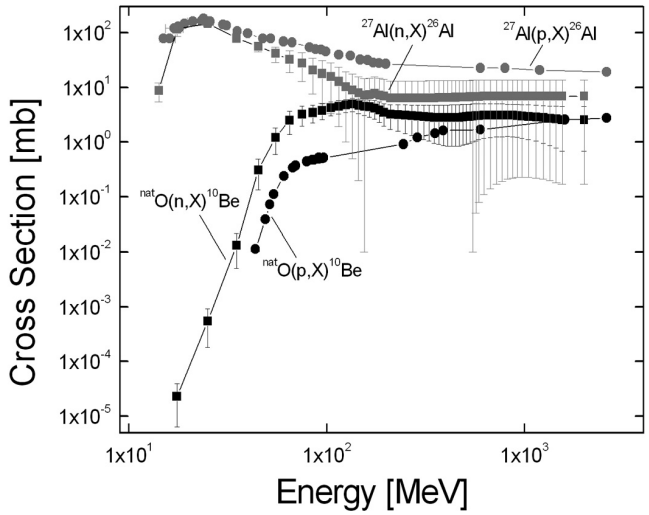

Fig. 1. Proton and neutron cross sections for the production of ^{10}Be from O and ^{26}Al from Al. The data demonstrate that the often used assumption of equal cross sections for proton and neutron induced reactions is generally not valid.

and L chondrites (e.g., Kollàr et al. 2006). Notable exceptions to the observation that the matrix effect is limited to thermal neutrons are carbonaceous chondrites, for which this effect is substantial even for intermediate energy particles. We therefore present here production rates for C chondrites and we discuss the matrix effect separately below. The chemical compositions used for the Monte Carlo calculations are compiled in Table 1. The uncertainties of the simulated particle spectra for protons and neutrons are estimated to be about 5%. Note that all particle spectra are normalized to an integral flux of primary GCR protons $J_{0,pp}$(E > 10 MeV) = 1 cm^{-2} s^{-1}. By way of example we compare in Fig. 2 the differential flux densities for L and C chondrites and discuss the implications below.

In order to enable direct comparisons of meteorite data and model predictions, the mean GCR spectrum in the meteoroids orbits, i.e., the mean number of primary GCR particles per area and time, has to be known (see also Leya et al. 2000a). We determined the integral number of primary GCR particles by comparing measured and modeled ^{10}Be and ^{26}Al depth profiles for the well studied L chondrite Knyahinya. This meteorite is well suited for such a comparison, because its preatmospheric shape and size have been carefully reconstructed (Graf et al. 1990a, 1990b). In addition, the exposure age of about 40 Ma and the fact that Knyahinya is a fall warrants that all radionuclides are in saturation. There is no indication of a complex exposure history and, due to the large radius of Knyahinya of ~45 cm, the production rates and therefore our determination of $J_{0,GCR}$ are not very sensitive to uncertainties of the radius determination. This is due to the fact that for meteoroids in this size range the production rates depend only minor on the size of the object. For example, the ^{26}Al production rate at the center of an ordinary chondrite with a radius of 25 cm is about 10% higher than at the center of a 20 cm meteoroid. In contrast, the production rates in the center of a 45 cm and 50 cm meteoroid are almost the same (<2%). Therefore, uncertainties in the radius determination have only minor effects for larger meteorites, which results in a relatively robust determination of $J_{0,GCR}$. The result of our $J_{0,GCR}$ determination is shown in Fig. 3. The experimental ^{10}Be data (Graf et al. 1990b) are reduced by 6.3%, because all input data used for modeling are based on the standard "S433" but the ^{10}Be data measured in Knyahinya are based on the standard "11a", which gives ^{10}Be activities 6.3% higher (Hofmann et al. 1987). Our best estimate for the integral number of GCR particles in the meteoroid orbit is 4.47 cm^{-2}s^{-1}, which is equivalent to a solar modulation parameter M of about 500, very similar to the value of M = 550 used by us for the LAHET calculations. Note that Ammon et al. (2008a) used the same $J_{0,GCR}$ to successfully describe cosmogenic production rates in iron meteorites. We note that with the current version of model calculations, though not yet perfect, it is for a first time possible to simultaneously model production rates in stony and iron meteorites with only one free parameter, the integral number of GCR particles in the meteoroid orbits (see Fig. 3).

PRODUCTION RATES FOR COSMOGENIC NUCLIDES

Due to the large number of calculations performed in this study we give the elemental production rates for ordinary chondrites ("OC") and carbonaceous chondrites ("CC") only as Excel files on our website http://www.noblegas.unibe.ch or upon request from the corresponding author. We prepared four Excel files, i.e., "Prts_OC_Radionuclides.xls" and "Prts_OC_NobleGases.xls" for the elemental production rates of cosmogenic radionuclides and noble gases in ordinary chondrites, respectively, and "Prts_CC_Radionuclides.xls" and "Prts_CC_NobleGases.xls" for the respective data for carbonaceous chondrites. In addition to the elemental production rates for all radii and shielding depths, these tables also contain for each target product combination a quality factor, with *A* being the highest and *E* being the lowest quality of modeling. The quality factors are defined as follow:

Quality factor A: for the proton-induced production there exist experimental cross sections from more than one group, all giving a reliable and consistent excitation function. There exist reliable and consistent thick target production rates from more than one simulation experiment. Combining all data results in a reliable neutron excitation function, i.e., the threshold energy is accurately given, the shape of the excitation function is physically reasonable, and the adjustment procedure changes the absolute cross sections of the guess function only slightly. Examples are ^{26}Al from Si and ^{10}Be from O.

Table 1. Chemical composition of H, L, LL, and C chondrites and for chondritic metal used for modeling.

Element	H chondrite	L chondrite	LL chondrite	C chondrites	Metal
H	–	–	–	2.0	
C	0.11	0.09	0.12	3.2	
N					
O	35.7	37.7	40.0	46.0	
Na	0.64	0.70	0.71	0.49	
Mg	14.0	14.9	15.3	9.7	
Al	1.13	1.22	1.19	0.86	
Si	16.9	18.5	18.9	10.5	
S	2.0	2.2	2.3	5.9	
Ca	1.25	1.31	1.30	0.92	
K*	800	870	910		
Ti	0.06	0.06	0.06	0.04	
Mn	0.23	0.26	0.26	0.19	
Fe	27.5	21.5	18.5	18.2	95.0
Ni	1.6	1.2	1.0	1.1	5.0
Ba*	4.1	3.7	4.8	2.41	
Te*	0.30	0.48	0.55	2.27	

The target element abundances used for the model calculations are from Mason (1979) and Jarosevich (1990) for H, L, and LL chondrites and from Palme and Jones (2003) for C chondrites.

*Concentrations are given in ppm.

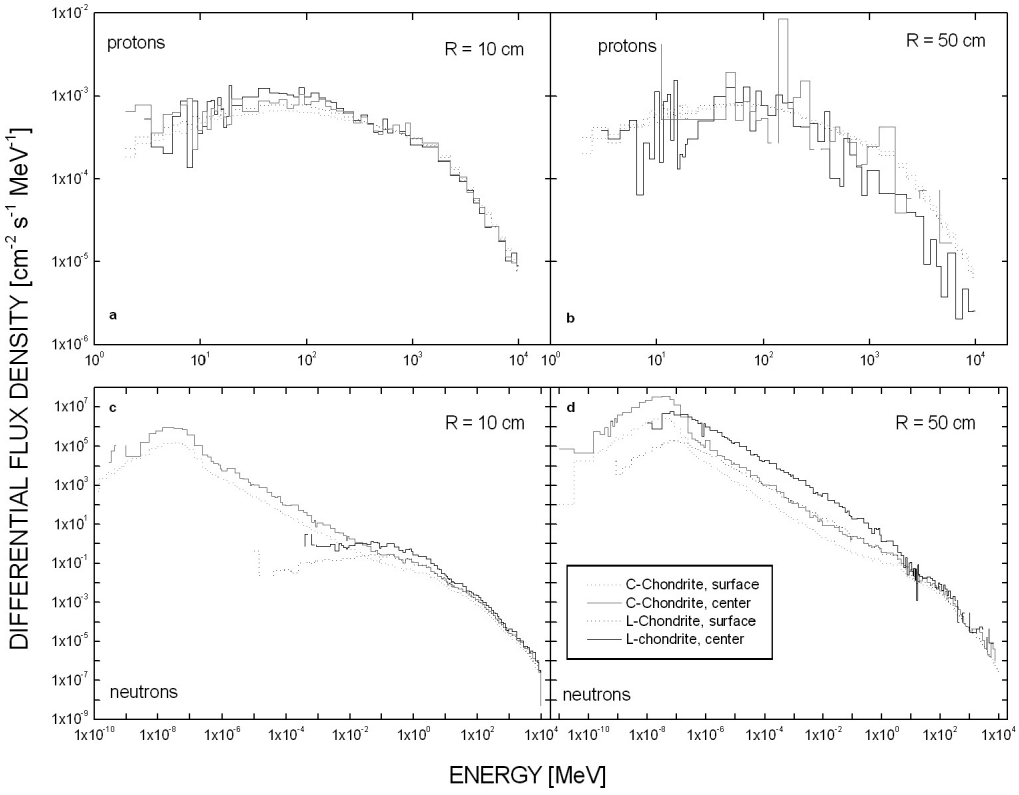

Fig. 2. Spectra of protons (primary + secondary) and secondary neutrons at the surface (dotted lines) and the center (solid lines) of 10 cm and 50 cm L and C chondrites. All data are normalized to an incident flux of primary galactic particles of 1 $cm^{-2}s^{-1}$.

Quality factor B: for the proton-induced production there exist only few experimental data and/or data from only one group and/or thick target production rates exist only for one simulation experiment. The neutron excitation function is nevertheless reliable, i.e., the shape is physically reasonable and the adjustment procedure results in only little changes of the guess function.

Quality factor C: the proton cross sections are scarce and scattering, i.e. they often disagree by up to a factor of 2, and/or the thick target production rates, if any, are questionable,

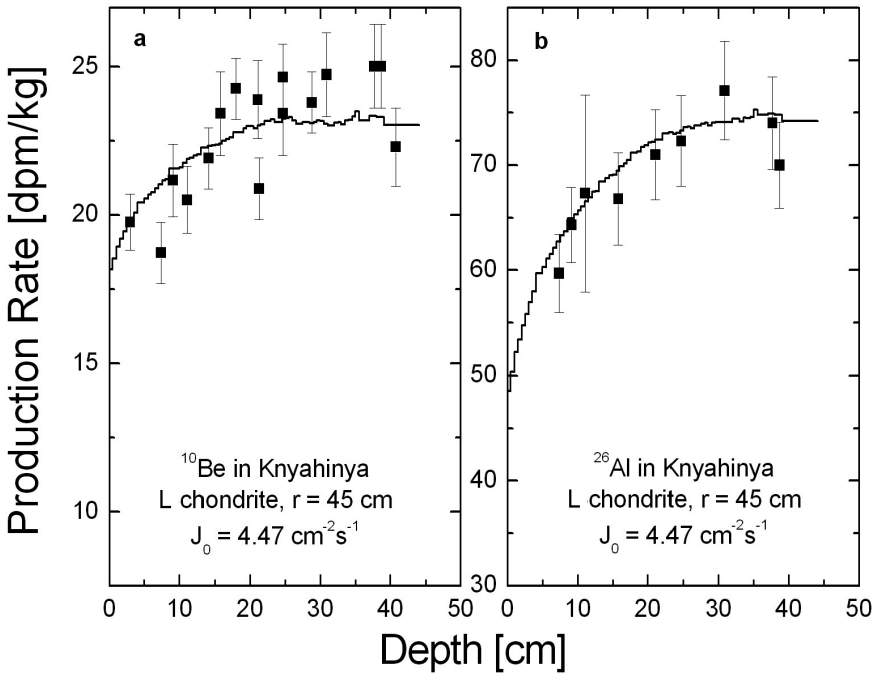

Fig. 3. Depth profiles of ^{10}Be and ^{26}Al in Knyahinya. The experimental data (Graf et al. 1990b; Vogt 1988) are used to determine the integral number of GCR particles by fitting the modeled depth profiles to the measured data.

i.e. not all thick target simulation experiments could be considered for the adjustment procedure and/or the a posteriori neutron excitation function differs by a factor of a few from the guess function.

Quality factor D: some proton cross sections exist, but no production rates from thick target simulation experiments. Therefore, the model calculations are based on a priori neutron cross sections, which have been calculated using the TALYS code or which have somehow been deduced from the cross sections for the proton-induced reaction.

Quality factor E: the model calculations are based on a priori proton and neutron cross sections.

We give here only quality factors from *A–E* for the model predictions because it is impossible to give a more quantitative estimate. A low quality factor, e.g., an *E*, does not automatically imply that the modeled production rates are wrong; it only indicates that we are not sure how reliable they are. Consequently, model predictions with a low quality factor should not be discarded, otherwise we would not give the data, but should be discussed carefully.

Production Rates of Cosmogenic Radionuclides

In Fig. 3, we compare measured and modeled rates for the ^{10}Be production in Knyahinya. The new model predictions describe the experimental data within their uncertainties, which is of no surprise because the production rates for ^{10}Be and ^{26}Al have been used to determine the $J_{0,GCR}$ value (see above). Note, however, that the good agreement between measured and modeled production rates for both, ^{10}Be and ^{26}Al is an indication for the good quality of the model predictions. Therefore, the systematic underestimation of the ^{10}Be production rates, from which our earlier model predictions suffered (Leya et al. 2000a), no longer exists. Panels a and b of Fig. 5 show the production rates of ^{10}Be in H chondrites with radii of 10, 20, 25, 30, 35, 40, 50, 65, 85, 100, and 120 cm on a lin-lin scale (panel a) and for radii of 120, 150, 200, 300, and 500 cm on a log-lin scale (panel b). The respective data for C chondrites are shown in panels c and d. The scatter in the production rates in the center of large objects, i.e., for radii larger than 1 m, is due to statistical reasons, i.e., limitations on computer time and hence on the propagation of secondary particle fluxes, and has no physical meaning. The ^{10}Be production rates in H chondrites increase from surface to center for radii less than about 50 cm. The production rates for larger objects increase with increasing depth at regions close to the surface, reach a local maximum, and start to decline towards the center. At the same time, the position of the local maximum moves closer to the surface with increasing radius. The highest production rates are reached in the center of a 50 cm object with ~21 dpm/kg. As can be seen in Fig. 5, the ^{10}Be depth profiles in C chondrites differ substantially from those in H chondrites. For C chondrites, the ^{10}Be production increases with depth for radii up to 85 cm and highest production rates are reached in the center of a 65 cm object. Furthermore, ^{10}Be production in C chondrites is significantly higher than in H chondrites. Note that all input data used for ^{10}Be modeling are based on the AMS standard “S433”. If the meteorite data are based on a

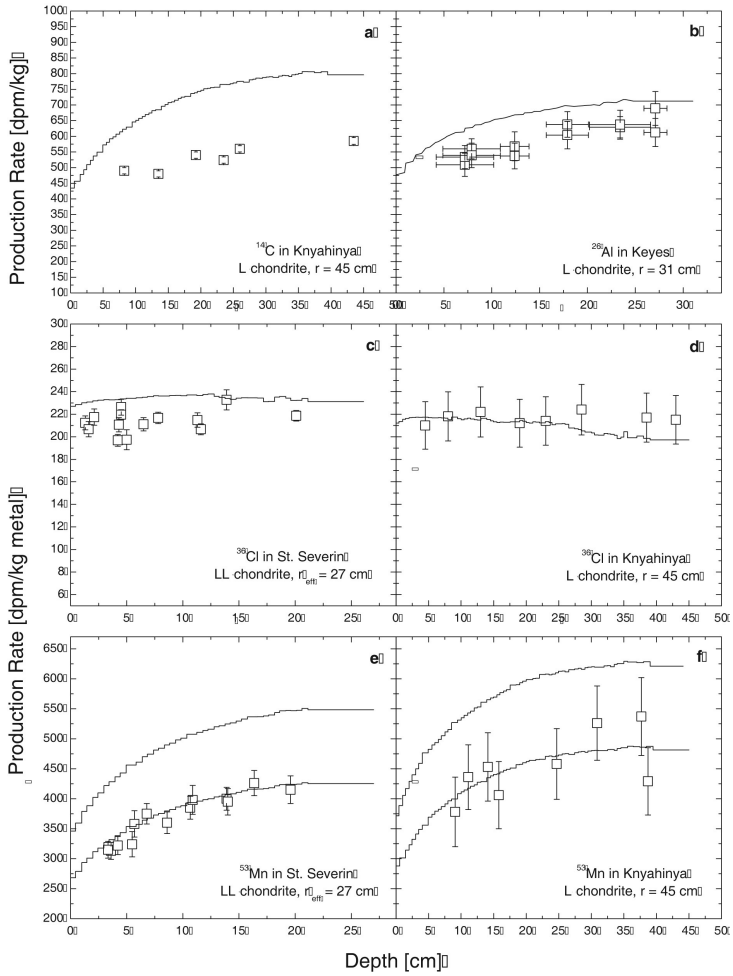

Fig. 4. Depth profiles of ^{14}C in Knyahinya, ^{26}Al in Keyes, ^{36}Cl in St. Severin and Knyahinya, and ^{53}Mn in St.Severin and Knyahinya. For reasons not yet understood, the model predictions overestimate the measured ^{14}C production rates by about 40%. For ^{36}Cl measured and modeled, data agree within the experimental uncertainties. For ^{53}Mn the modeled data overestimate the experimental data by about 30%, which is due to the different standards used. Whereas all input data used for modeling are based on a new AMS standard, the ^{53}Mn data for St. Severin and Knyahinya were obtained by neutron activation techniques using a different standard. The experimental data are from Cressy (1975), Englert and Herr (1980), Nishiizumi et al. (1989), Reedy et al. (1993), and Vogt (1988).

standard which differ from "S433," as, for example, the ^{10}Be data in Knyahinya, which are based on the standard "11a," a renormalization of either the model or the experimental data is necessary.

In Fig. 4a, we compare measured and modeled ^{14}C depth profiles for the L chondrite Knyahinya. For reasons not yet understood, the model calculations overestimate the experimental data by about 40%. The cross sections for the proton-induced reactions are relatively well known and for oxygen, which is the main target element, we also have a posteriori neutron excitation functions (Quality factor B). It is therefore hard to understand why the production rates from oxygen alone are already higher than the total production rates for Knyahinya. A possible, but unlikely explanation, might be that the GCR flux density during the last 20 ka has been lower than the long term average by about 40%. However, at present we cannot explain the discrepancy and for practical applications the model predictions have to be reduced by a factor of 1.4. Since such adjustments contradict our idea of a purely physical model, further cross section measurements and a check of the ^{14}C depth profile of Knyahinya, which has not be reproduced so far, and probably the measurement of more depth profiles for other well studied meteorites like Keyes and St. Severin are needed.

In Figs. 3b and 4b, we compare modeled and measured ^{26}Al depth profiles for Knyahinya and Keyes, respectively. For Knyahinya the agreement between model predictions and measured data is good; not a surprise since these data have been used to determine the $J_{0,GCR}$ value. That the shape of the measured depth profile is well reproduced validates the model. For Keyes, however, the model predictions are about 10% higher than the measured data (Cressy 1975), which, though not completely satisfying, is well within the range of uncertainties assumed for the

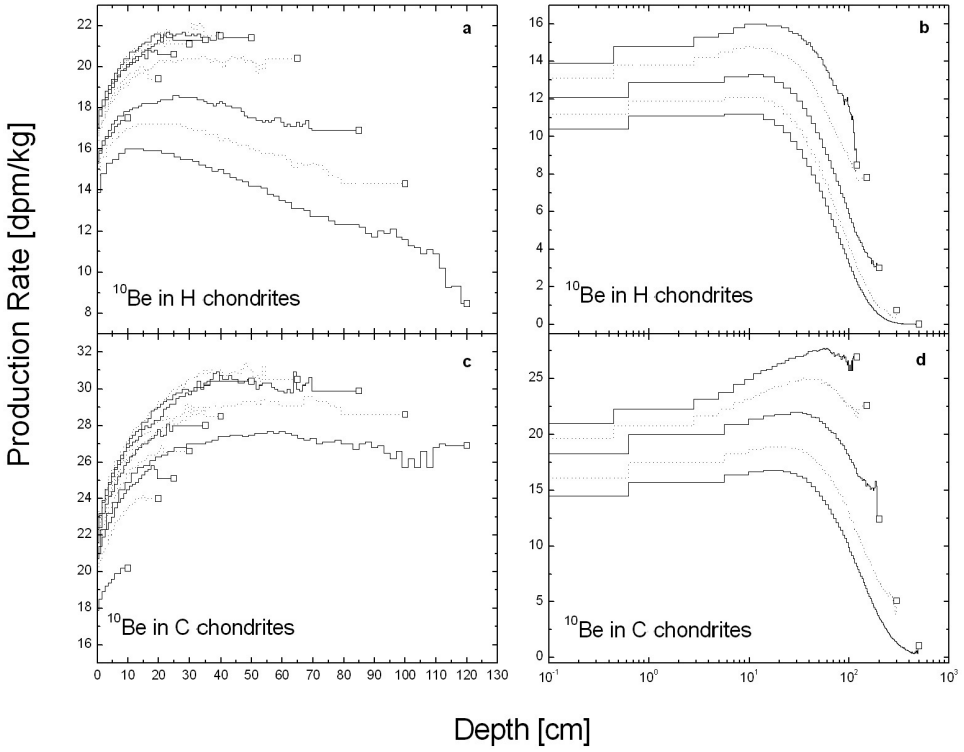

Fig. 5. Galactic cosmic-ray production rates of ^{10}Be in H chondrites (upper panels) and C chondrites (lower panels) with radii between 10 cm and 120 cm (left panels), and between 120 cm and 500 cm (right panels).

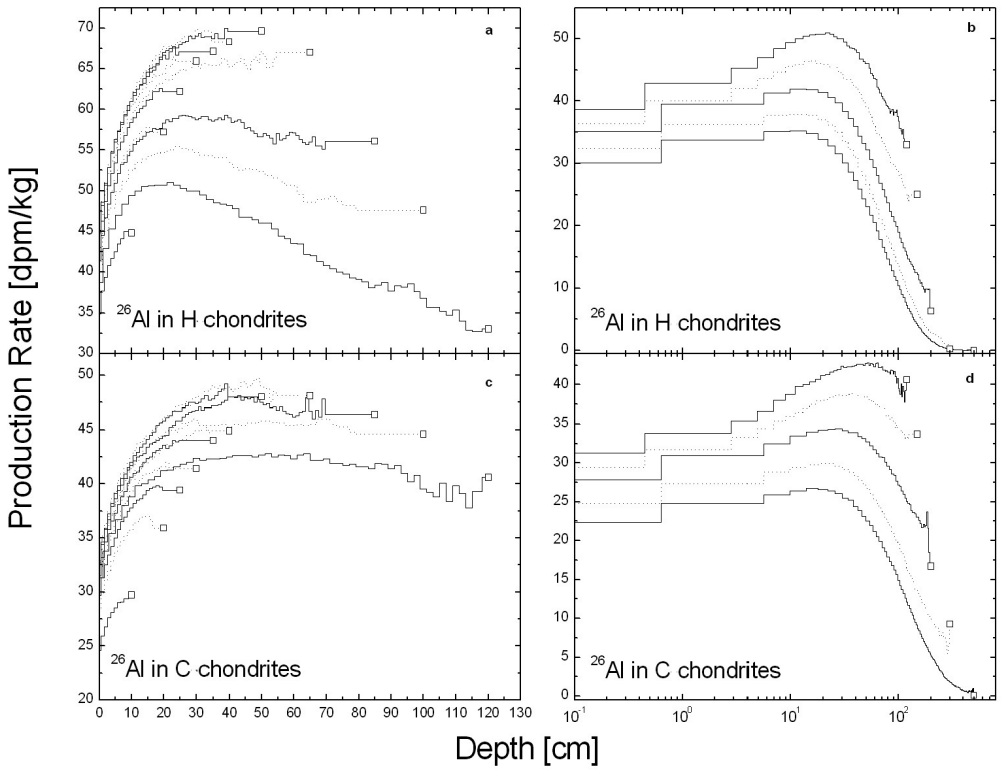

Fig. 6. Galactic cosmic-ray production rates of ^{26}Al in H chondrites (upper panels) and C chondrites (lower panels) with radii between 10 cm and 120 cm (left panels) and between 120 cm and 500 cm (right panels).

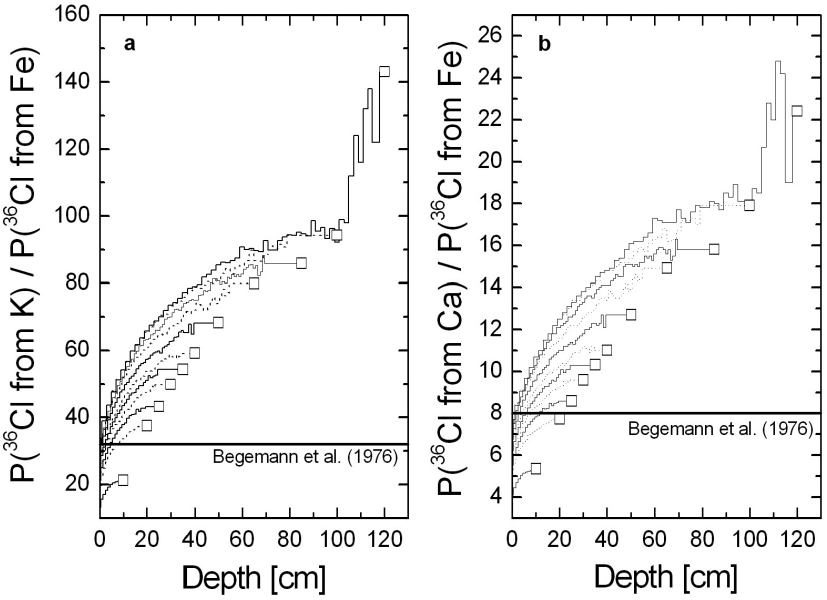

Fig. 7. Production rate ratios P(^{36}Cl from K)/P(^{36}Cl from Fe) (left panel) and P(^{36}Cl from Ca)/P(^{36}Cl from Fe) (right panel). Also shown are the ratios deduced by Begemann et al. (1976) for stony-iron meteorites. The model predictions show that the ratios determined by these authors are reached only in ordinary and carbonaceous chondrites with radii below 10–20 cm. In chondrites larger than ~10 cm, the production rate ratios are significantly higher. Furthermore, the model predictions demonstrate that both production rate ratios depend on the size of the meteorite and the shielding depth of the sample.

model calculations (see below). Again, the shape of the experimental depth profile is well reproduced by the model. The ^{26}Al production rates in H and C chondrites with radii between 10 cm and 500 cm are shown in Fig. 6. The ^{26}Al depth profiles in H chondrites increase from the surface towards the center and reach maximum values at the center of a 50 cm object. For larger objects the production peaks close to the surface followed by an almost exponential decrease with increasing shielding. For C chondrites the production rates near the surface are significantly lower than those in H chondrites, but also reach maximum values at the center of about 50 cm objects. For larger objects, however, the decrease with depth is in C chondrites less pronounced than in H chondrites.

Modeled ^{26}Al/^{10}Be ratios in the metal phase of ordinary chondrites with radii between 10 and 120 cm are between 0.74 and 0.87, i.e., in good agreement with the ratio of 0.71 ± 0.05 measured for the Brenham pallasite (Honda et al. 2002) and also consistent with many studies of iron meteorites (e.g., Aylmer et al. 1988; Nagai et al. 1993; Lavielle et al. 1999).

In Figs. 4c and 4d, we compare measured and modeled ^{36}Cl production rates for St. Severin and Knyahinya, respectively. For the latter meteorite, the agreement between model predictions and measured data is good, i.e., within the uncertainties of the experimental data, but for St. Severin the modeled data are slightly too high by about 10%, which is, however, again in the range of the uncertainties assumed for the model predictions. For modeling production rates in metal, we assume a chemical composition of 95% Fe and 5% Ni (Mason 1979). Figure 7 shows elemental production rate ratios P(^{36}Cl from K)/P(^{36}Cl from Fe) and P(^{36}Cl from Ca)/P(^{36}Cl from Fe) as a function of radius and depth for L chondrites with radii between 10 cm and 120 cm. Along with the model predictions we also show the production rate ratios deduced by Begemann et al. (1976) for stony-iron meteorites. It can be seen that most of the model predictions are higher than the estimates by Begemann et al. (1976). For example, while the latter authors predict a P(^{36}Cl from K)/P(^{36}Cl from Fe) ratio of 32, we model ratios between ~20 for small objects and ~70 for meteoroids with a radius of 50 cm; the majority of our data gives a ratio of about 60. Our modeled P(^{36}Cl from Ca)/P(^{36}Cl from Fe) ratios are between ~5 for small meteoroids and ~10 for objects with 50 cm radius. In contrast, Begemann et al. (1976) published a ratio of 8, independent of size and shielding depth. Note that both production rate ratios are expected to vary with size and depth. While the production of ^{36}Cl from Fe has a threshold energy of about 100 MeV and is therefore dominated by rather high energy projectiles, the production of ^{36}Cl from K and Ca starts at about 20 MeV, making it a low to medium energy reaction. Consequently, while ^{36}Cl production from Fe decreases with shielding, the production of ^{36}Cl from K and Ca increases with shielding. Consequently, the elemental production rate ratios are expected to vary with shielding, as shown in Fig. 7.

The depth- and size-dependent production rates for ^{41}Ca produced in the metal phase of ordinary (upper panels) and carbonaceous chondrites (lower panels) are shown in Fig. 8. Note that the lack of measured ^{41}Ca data for samples with known shielding conditions prevents a direct evaluation of the model predictions. However, the modeled average ^{41}Ca/^{36}Cl

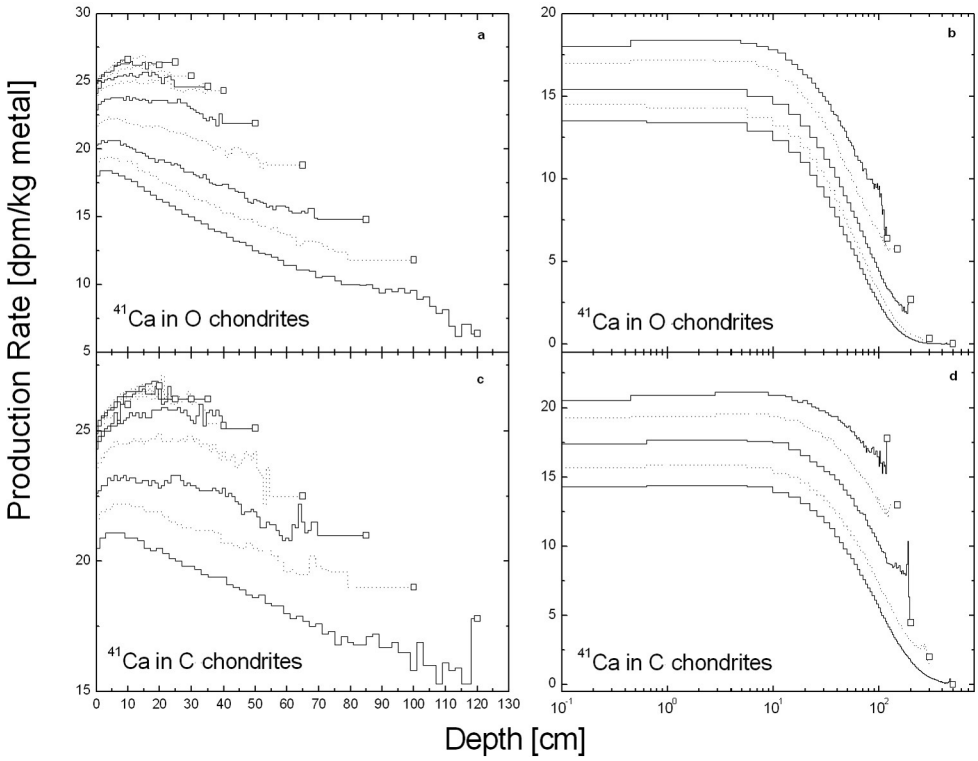

Fig. 8. Galactic cosmic-ray production rates of ^{41}Ca in the metal of ordinary chondrites (upper panels) and carbonaceous chondrites (lower panels) with radii between 10 cm and 120 cm (left panels), and between 120 cm and 500 cm (right panels).

ratio of ~1.2 for the metal phase of ordinary chondrites with radii between 10 cm and 200 cm agrees reasonably well with data for the large L chondrite Gold Basin, for which average ^{41}Ca/^{36}Cl ratios of ~1.12 have been measured (Welten et al. 2003). In addition, the absolute values of the modeled ^{41}Ca production rates of about 24 dpm/kg(metal) for a meteoroid with a radius of about 60 cm is in good agreement with data for e.g., Jilin, which has a measured saturation activity of ~24 dpm/kg(metal) (e.g., Klein et al. 1991).

In Figs. 4e and 4f we compare measured and modeled ^{53}Mn depth profiles for Knyahinya and St. Severin, respectively. In contrast to our earlier model, which accurately predicts the ^{53}Mn data, the new calculations significantly overestimate them. This discrepancy is due to the fact that all input data used for modeling are now normalized to a new AMS standard and a new half-life for ^{53}Mn (Knie et al. Forthcoming; Merchel personal communication), which increases the all cross sections and thus the model predictions by about 29% compared to the earlier version. In contrast, the ^{53}Mn data in Knyahinya have been obtained by radiochemical neutron activation techniques and are normalized to the standard Bogou II from K. Nishiizumi and a standard prepared at the University of Cologne (Sarafin 1985). For St. Severin the ^{53}Mn data are also obtained by neutron activation techniques but they are normalized only to the standard Bogou II (Bhattacharya et al. 1980). Consequently, the renormalization of the ^{53}Mn AMS standard only affects the input data used for modeling but not the meteorite data. The discrepancy between model predictions and meteorite data therefore indicate that both standards, Bogou-II and the new AMS standard, differ by about 30%. We currently plan to solve this problem by measuring ^{53}Mn in a documented Knyahinya sample using the new AMS standard. Clearly, in the case of ^{53}Mn data, it is essential to check which standard (and which half-life) has been used and—if necessary—a renormalization of either data must be performed.

Validating the model calculations for ^{60}Fe in stony meteorites is currently impossible due to the lack of experimental meteorite data. For ordinary chondrites with radii less than about 60 cm ^{60}Fe production increases from the surface towards the center. For larger objects, the production rates reach a local maximum of ~0.71 dpm/kgNi close to the surface and then (almost) exponentially decrease with increasing shielding depth. Maximum values of about 0.7 dpm/kgNi are reached in central regions of objects with radii between 40 and 50 cm. In C chondrites with radii less than about 1 m the ^{60}Fe depth profiles increase from the surface toward the center. For larger objects, i.e., for radii larger than 2 m, a local maximum of ~0.4 dpm/kgNi close to the surface builds up followed by production rates which (almost) exponentially decrease toward higher shielding depths. Comparing the ^{60}Fe production in ordinary and carbonaceous chondrites we see that the production rates for

ordinary chondrites are higher than those of carbonaceous chondrites for objects smaller than about 85 cm, whereas the differences between both chondrite types increase with increasing shielding for a given radius. For larger meteorites, the values in carbonaceous chondrites are higher than in ordinary chondrites, e.g., by up to a factor of 2 in the center of a 3 m object. Ammon et al. (2008a) showed that the model predictions for ^{60}Fe in iron meteorites underestimate the (very few existing) experimental data by up to a factor of 2 (Ammon et al. 2008a).

For ^{129}I the new model calculations update our earlier estimates (cf. Schnabel et al. 1998, 2004). In large meteoroids a significant part of ^{129}I is produced via neutron capture on ^{128}Te with subsequent α-decay. For reasons not yet understood, and as observed previously (e.g., Leya et al. 2001, Kollàr et al. 2006), the model is not able to simultaneously describe production rates for neutron capture and spallation reactions with the same set of input-parameters (e.g., Kollàr et al. 2006). While cosmogenic nuclides produced via spallation reactions are best described using $J_{0,GCR}$ = 4.47 cm^{-2}s^{-1} (see above), products produced via neutron capture reactions can only be described using $J_{0,GCR}$ = 2.99 cm^{-2}s^{-1} (Kollàr et al. 2006). The reason for this 50% discrepancy is not yet understood and further studies are needed. For practical applications, however, we use the respective $J_{0,GCR}$ values for neutron capture and spallogenic produced nuclides to determine the total ^{129}I production rates. For the spallogenic production of ^{129}I from Te an experimental neutron cross section at 14.7 MeV exists (Schnabel et al. 2000), making this elemental production rates relative reliable (Quality factor A). In contrast, the situation for the thermal neutron capture production of ^{129}I from ^{128}Te is far from satisfying, because the production rates significantly depend on the cross section database used for modeling. For example, Kollàr et al. (2006) showed that the capture rates for chondrites with radii >70 cm and for shielding depths >60 cm calculated using JEF-2.2 (Joint Evaluated File) are about 27% lower than those calculated using ENDF/B data (Evaluated Nuclear Data File version B-Brookhaven). In smaller objects and shallower shielding depths the differences are depth- and size-dependent, and reach up 50%. The difference caused by the two different cross section data sets is due to the fact that a wider resonance region is resolved in JEF compared to ENDF/B and, in addition, there is also a considerable difference in the cross section data right above the resonances. However, due to the fact that thermal neutron capture reactions are only of minor importance in small objects, the large differences (up to 50%) have no practical relevance. In contrast, the 27% effect for high shielding depths and in large objects directly compromises our interpretation of ^{129}I production rates in such objects, because its production in them is dominated by thermal neutron capture.

Schnabel et al. (2004) measured a ^{129}I production rate of (3.30 ± 0.25) × 10^{-4} dpm/kg in a Knyahinya sample with a shielding depth of about 10 cm. Assuming 6260 µg/kg Ba and 526 µg/kg Te (cf. Schnabel et al. 2004), the modeled production rate is ~3.31 × 10^{-4} dpm/kg, which is in perfect agreement. In a 13 cm deep sample of the EH4 chondrite Abee, which had a preatmospheric radius of ~30 cm (Goswami 1983), Nishiizumi et al. (1983) measured a ^{129}I production rate of 1.4 × 10^{-3} dpm/kg. Assuming 2.40 mg/kg Te and 3.15 mg/kg Ba we model production rates between ~4 × 10^{-4} dpm/kg at the surface and ~1.3 × 10^{-3} dpm/kg at the center, which is in reasonable agreement with the experimental data. For a sample of the CV3 chondrite Allende, Nishiizumi et al. (1983) measured a production rate of 9.3 × 10^{-4} dpm/kg. Using Te and Ba concentrations of 1.02 mg/kg and 4.9 mg/kg, respectively (Wasson and Kallemeyn 1988), we model for the same shielding conditions (R = 85 cm, d = 30 cm) a production rate of only 4.46 × 10^{-4} dpm/kg, i.e. about a factor of two lower than the experimental value. The new model prediction for Allende is substantially different from our earlier estimate (Schnabel et al. 2004), which is due to the fact that in the current study we use particle spectra for C chondrites, whereas in our earlier approach we approximated the spectra for C chondrites with spectra for H chondrites, which was obviously not correct. With L-chondrite spectra we calculate a production rate of 1.3 × 10^{-3} dpm/kg. This value is substantially higher than the one calculated using the correct spectra for C chondrites, but nonetheless in reasonable agreement with our earlier estimate (Schnabel et al. 2004) and—to our surprise—in better agreement with the experimental data, i.e., within 40%.

For modeling the ^{129}I production caution is necessary: production of ^{129}I in stony meteorites is exclusively from Ba and Te, both are trace elements. Therefore, sample inhomogeneities, which are of minor importance for nuclides produced from major target elements, are a major concern for nuclides produced from trace elements. Consequently, inhomogeneous distribution of Ba and Te directly translates into ^{129}I production rate variations, which are therefore expected to be much larger than for the other cosmogenic nuclides studied here.

Production Rates of Cosmogenic Noble Gases

The ^{3}He production rates for H and C chondrites with radii from 10 cm to 500 cm are shown in Fig. 9. For this modeling, the ^{3}H/^{3}He branching ratios have to be known. Here we use ^{3}H/^{3}He ratios of 1.20 for Mg, 1.28 for Al, and 1.11 for Si, that have been determined by Leya et al. (2004a, 2008) from thick target simulation data and which are in good agreement with ratios measured at a proton energy of 1.2 GeV by Herbach et al. (2006). For Fe and Ni we use a ^{3}H/^{3}He ratio of 1.63 (Herbach et al. 2006). We use this value instead of the often used ratio of 2 (Hintenberger et al.

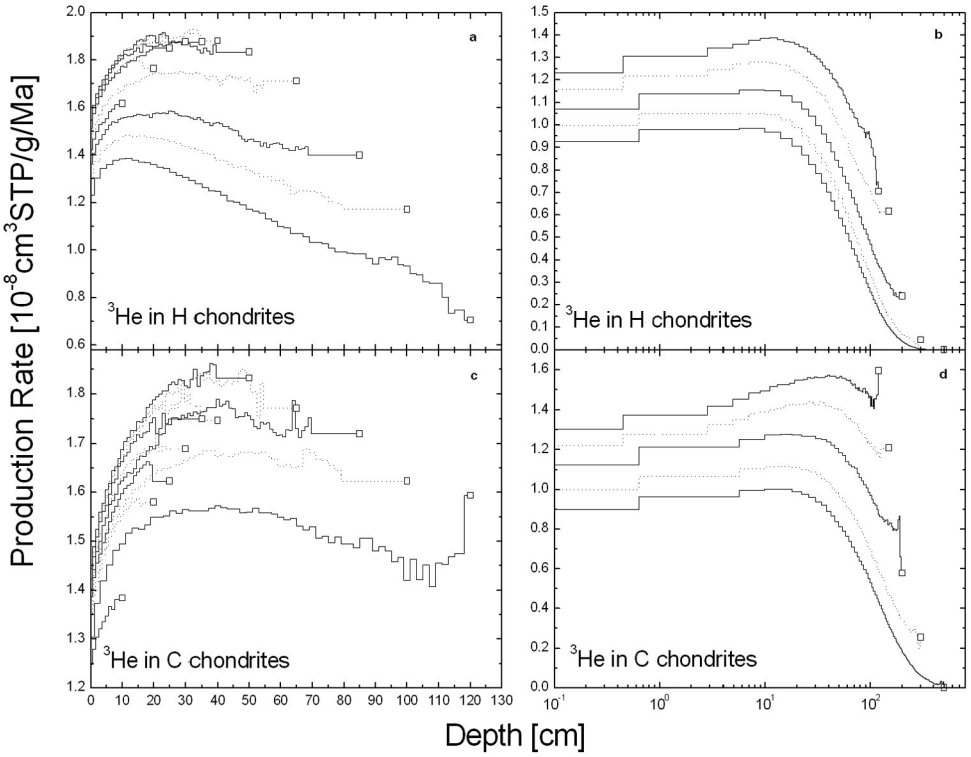

Fig. 9. Galactic cosmic-ray production rates of ^{3}He in H chondrites (upper panels) and C chondrites (lower panels) with radii between 10 cm and 120 cm (left panels), and between 120 cm and 500 cm (right panels).

1967), because the former has been determined in an independent setup based only on nuclear reaction data but the latter is empirically determined from meteorite data. The branching ratio for O, i.e., ^{3}H/^{3}He = 0.94, has been determined by linear extrapolation of ^{3}H/^{3}He versus mass number of the target elements, considering also elements up to Pb (Herbach et al. 2006). All input data used for modeling, i.e., the proton-induced cross sections and the thick target data used for determining neutron cross sections, are corrected for ^{3}H diffusive losses during irradiation and/or storage, which are substantial for some target elements, especially for Mg, Fe, and Ni. For the corrections we assume that the diffusive losses follow a simple exponential law with a constant D, i.e., we assume that the decrease of the ^{3}H concentrations due to diffusion can be described using e^{-Dt}. For the dimensionless ratio D/λ we use 2.6, 0.16, 0.014, and 2.4 for Mg, Al, Si, and Fe/Ni respectively, whereas λ (=1.027 × 10^{-6} s^{-1}) is the decay constant of ^{3}H (cf. Leya et al. 2004a).

The production rates for ^{21}Ne are shown in Fig. 10. To check the reliability of the model predictions we determined ^{21}Ne exposure ages for Knyahinya, Keyes, Bansur, Allan Hills (ALH) 78084, Udaipur, and St. Severin by fitting modeled ^{21}Ne depth profiles to experimental data. Doing so, we use the preatmospheric depths of the samples given by Graf et al. (1990b) and simply fitted for each sample the modeled data to the measured ^{21}Ne concentrations. The exposure age is then determined by calculating the mean value and the given uncertainty is the standard deviation of the mean. This approach is the most reliable one to determine cosmic-ray exposure ages for meteoroids having no complex exposure history. In Table 2 we compare the thus determined ages with ages derived from two empirical approaches (Nishiizumi et al. 1980; Eugster 1988) and a semi-empirical model (Graf et al. 1990a). Maximum differences are 18% but most ages agree to within better than 10%. For the L/LL5 chondrite Knyahinya our age of 34.8 ± 1.4 also agrees reasonably well with ^{81}Kr-Kr ages of 39.5 ± 1.0 Ma and 41.8 ± 0.8 Ma determined by Lavielle et al. (1997) and Leya et al. (2004b), respectively.

In addition to ^{21}Ne production rates for bulk chondrites we have also calculated elemental production rate ratios. The modeled P^{21}(Mg)/P^{21}(Si) ratios for ordinary chondrites with radii between 10 cm and 50 cm vary between 2.4 and 3.8 with an average value of 3.6. This is lower than the ratio of (6 ± 2) published by Begemann et al. (1976) and the values of (5.3 ± 3) and ($4.7^{+4.5}_{-2.5}$) derived by Bochsler et al. (1969) for Elenovka and Otis, respectively, and it is also lower than the ratios of (5.3 ± 1.8) and 6.8 published by Bogard and Cressy (1973) and Stauffer (1962), respectively. The variations with size and depth for the modeled P^{21}(Al)/P^{21}(Si) ratios are much smaller, i.e., they range only between 1.3 and 1.7 with an average value of 1.4 (again considering only meteoroids with radii between 10 cm and 50 cm). This value is

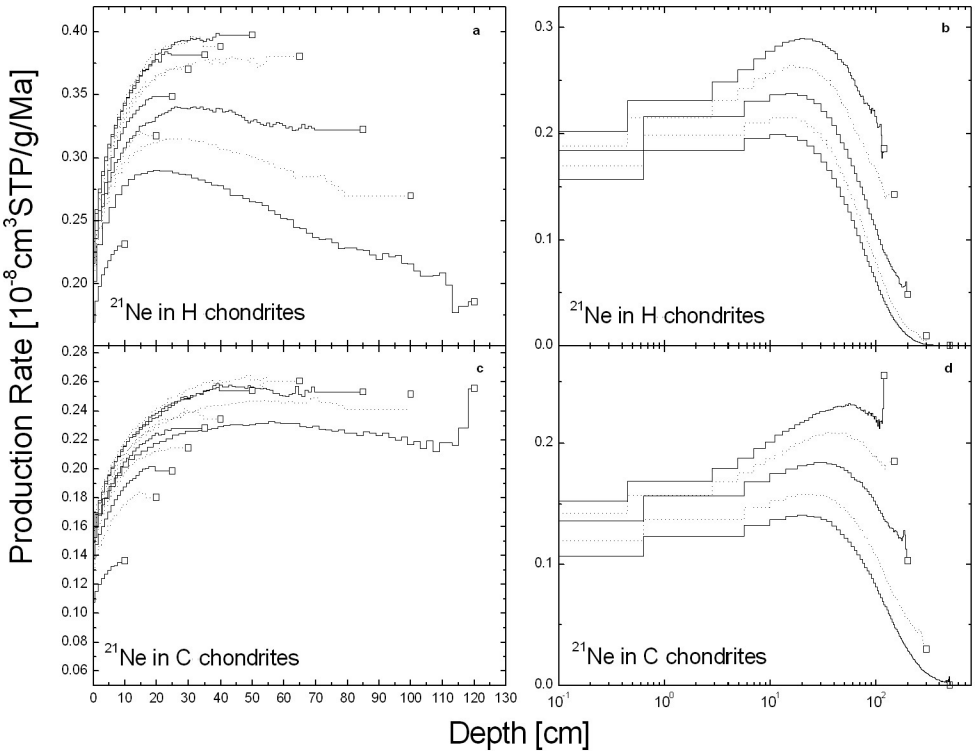

Fig. 10. Galactic cosmic-ray production rates of ^{21}Ne in H chondrites (upper panels) and C chondrites (lower panels) with radii between 10 cm and 120 cm (left panels), and between 120 cm and 500 cm (right panels).

significantly higher than the ratio of 0.5 ± 0.5 adopted by Begemann et al. (1976). However, for both elemental ratios we assume that our data are superior because they are based on very reliable input data for modeling and we fully consider, in contrast to the earlier authors, the depth and size dependence of the production rate ratios. As a final test for the modeled Ne data we compare measured and modeled ^{20}Ne/^{22}Ne ratios. Considering all sizes and shielding depths the modeled ^{20}Ne/^{22}Ne ratios are on average 0.78, which is in very good agreement with the ratio of 0.8 ± 0.3 obtained by Eugster et al. (2007) from a variety of meteorites. The model predictions for the shielding indicator ^{22}Ne/^{21}Ne are discussed in detail below.

We present ^{38}Ar depth profiles for H chondrites and carbonaceous chondrites in Fig. 11. The data are given together with the data for ^{36}Ar in the Excel sheet on our website. The current version of model calculations—in contrast to the previous version—is able to predict production rates from Ca, Fe, and Ni, which are the major target elements for Ar production in bulk chondrites as well as in the metal. We now consider for the ^{36}Ar productions rates the distribution along the isobar 36: While for metal about 85% of total ^{36}Ar is produced via ^{36}Cl, in the case of Ca this fraction is only about 30%. The model predicts ^{36}Ar/^{38}Ar ratios in metal of 0.7–0.9, which is significantly higher than the cosmogenic ^{36}Ar/^{38}Ar ratio of 0.63. Currently we have no explanation for this shortcoming, as most ^{36}Ar is produced via ^{36}Cl, which is properly described by the model, and the calculations for ^{38}Ar are also based on very reliable input data. However, the same shortcoming has recently been observed for iron meteorites and has been interpreted as most probably due to the fact that for modeling ^{36}Ar we have to mix data measured by AMS (^{36}Cl) with those measured by noble gas mass spectrometry (direct ^{36}Ar production), which might result in some problems due to the different standards used in each technique (e.g., Ammon et al. 2008a).

The modeled P^{38}(Ca)/P^{38}(Fe) ratios strongly depend, as expected, on meteoroid size and shielding depth and range between 12 for shallow shielding in small objects to, e.g., about 50 in the center of a 50 cm object. The modeled values are in reasonable agreement with the ratios of 27–41 given by Begemann et al. (1976) for stony-iron meteorites, 17 ± 2 determined by Bogard and Cressy (1973) for Bruderheim, and (20^{+20}_{-7}) and (37 ± 11) for the chondrites Otis and Elenovka, respectively (Bochsler et al. 1969). In reasonable agreement are also experimental and modeled ^{38}Ar production rates from Ca. While Begemann et al. (1976) determined (in 10^{-8}cm^{3}STP/g/Ma) values between 0.26 and 3.55, we model production rates between ~1 and 2.7 for chondrites with radii between 10 cm and 50 cm, respectively. The production rates given by Bochsler et al. (1969) of (3.3 ± 0.7) and (4.1 ± 1.2) are slightly higher than the model predictions. Also the P^{38}(Ca) value of 1.8 for lunar samples given by Huneke et al.

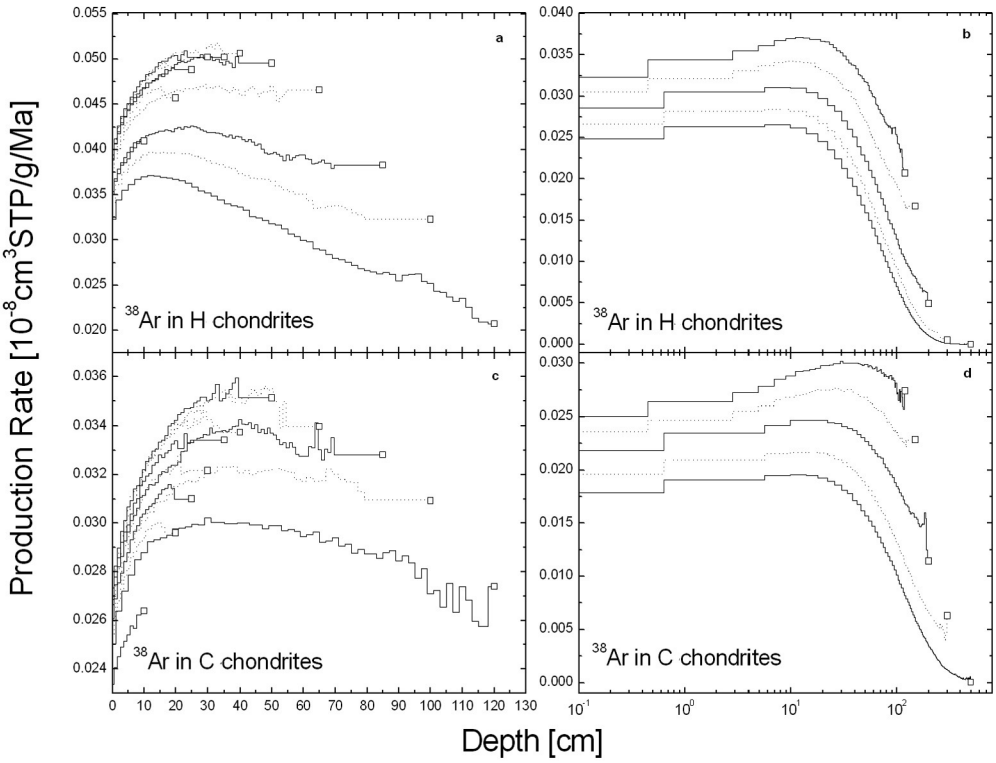

Fig. 11. Galactic cosmic-ray production rates of ^{38}Ar in H chondrites (upper panels) and C chondrites (lower panels) with radii between 10 cm and 120 cm (left panels), and between 120 cm and 500 cm (right panels).

Table 2. Cosmic-ray exposure ages for some ordinary chondrites.

Meteorite	R (cm)	T_{exp} (Ma) (Nishiizumi)	T_{exp} (Ma) (Eugster)	T_{exp} (Ma) (Graf)	T_{exp} (Ma) (via ^{21}Ne)	T_{exp} (Ma) (^{21}Ne- ^{22}Ne/^{21}Ne)
Knyahinya	45	40.3 (0.3)	37.7 (0.3)	40.5 (0.2)	34.7 (1.5)	36.0 (1.0)
Keyes	31	29.2 (0.3)	27.3 (0.2)	24.6 (0.2)	26.2 (0.7)	26.1 (0.5)
Bansur	14	24.2 (0.3)	22.6 (0.3)	–	24.3 (2.0)	23.5 (2.0)
ALH 78084	14	32.8 (0.4)	30.6 (0.3)	28.9 (0.3)	31.7 (0.9)	32.4 (1.2)
Udaipur	12	38.6 (0.5)	36.1 (0.5)	–	34.6 (0.5)	47.3 (0.6)
St. Severin	27	–	–	–	14.6 (0.5)	15.2 (0.8)

The noble gas data are from Graf (1988), Graf et al. (1990b), Cressy (1975), Gopalan and Rao (1976), Sarafin (1985), and Schultz and Signer (1976). For Knyahinya two ^{81}Kr-Kr ages exist: 39.5 ± 1.0 and 41.8 ± 0.8 Ma by Lavielle et al. (1997) and Leya et al. (2004b).

(1972) is higher than expected considering that the model predicts a maximum ^{38}Ar production rate from Ca of only 1.4 for a meteoroid with a radius of 500 cm. Note that such a comparison is a bit questionable, because we compare average values derived from empirical data to model predictions, which cover the whole size and depth spectrum.

As a crucial test for the quality of the model calculations we compare measured and modeled ^{3}He/^{38}Ar in metal. This ratio is of special interest because it is often used to estimate ^{3}H and/or ^{3}He diffusive losses. Considering only ordinary chondrites with radii between 10 cm and 120 cm we model ^{3}He/^{38}Ar ratios between 15–21. The average value (considering all shielding depths) of 17 is in good agreement with the ratio of 16 assumed in most cosmogenic nuclide studies (cf. Signer and Nier 1962; Lipschutz et al. 1965; Schultz and Hintenberger 1967; Nyquist et al. 1973; Begemann et al. 1976).

As a final test, we compare measured and modeled P^{21}(Mg)/P^{38}(Ca) ratios. Considering all shielding depths in L chondrites with radii between 10 cm and 50 cm we model ratios of ~0.7, which is in good agreement with the value of about 1 determined by Begemann et al. (1976) for stony-iron meteorites and with the ratios of 1.23 ± 0.17, 0.54 ± 0.17, and 0.67 ± 0.18 determined by Bogard and Cressy (1973) for Bruderheim, and by Bochsler et al. (1969) for Elenovka and Otis, respectively. Finally we also compare measured and modeled ^{21}Ne/^{38}Ar ratios in the metal phase of ordinary chondrites. This ratio is often used to determine the degree of silicate contamination of separated metal samples. The model predicts ratios

between 0.16 and 0.25 with an average of 0.20 (for all shielding depths in objects with radii between 10 cm and 50 cm), which is in good agreement with the value of 0.15 used in various cosmogenic nuclide studies (cf. Begemann et al. 1976; Signer and Nier 1962; Schultz and Hintenberger 1967; Nyquist et al. 1973).

THE MATRIX EFFECT

The elemental production rates not only depend on radius and shielding depth but also on the chemical composition of the irradiated object, the so-called matrix effect (cf. Begemann and Schultz 1988; Masarik and Reedy 1994). The existence of this effect has several causes. First, the production of secondary particles depends on the mass number of the target atoms. The number of emitted particles in a nuclear reaction is, for a fixed projectile energy, roughly proportional to the mass number of the target (e.g., Carpenter 1987; Pearlstein 1987). Consequently, the production of secondary particles in iron meteorites is more than two times higher than in chondrites. Second, the energy of the particles emitted in a nuclear reaction depends on the mass number of the target atoms. As an example, we consider an individual nuclear reaction. After the absorption of the projectile the number of interactions within the target nucleus (intranuclear cascade) is proportional to $A^{0.31}$, with A the mass number (Feshbach 1992). Consequently, there are on average 30% more interactions in iron meteorites ($A^{0.31}$ = 2.44) than in chondrites ($A^{0.31}$ = 1.9). Since in each interaction about half of the energy is transferred, the more interactions the lower the probability of high energy secondary particles. Consequently, there are more secondary particles in an iron meteorite but they have (on average) lower energies than the (fewer) secondary particles in stony meteorites like chondrites. Third, stopping of primary and secondary protons as well as moderation of secondary neutrons also depend on the mean mass number of the irradiated object. While stopping of charged particles is higher in objects having a high mass number, neutron moderation is much more efficient in targets having a low mass number.

For a proper interpretation of the matrix effect, shielding depths and radii have to be discussed in the unit (g/cm^2), because the densities, and with them the number of target atoms per unit volume, vary significantly between different types of meteorites. Note that a rigorous treatment of production and transport of secondary particles would use, instead of the unit (g/cm^2), the macroscopic inelastic cross section times depth. In such a depth scale, the attenuation of primary particles is almost the same at the same depth no matter the chemical composition of the target. Consequently, a discussion based on such scale would enable one to directly compare effects only due to secondary particles. Here we use nevertheless the depth scale (g/cm^2), because it is widely used for meteorites and it is also well suited for a proper discussion of the matrix effect.

Here we discuss the matrix effect for H, L, and LL chondrites. For all three types of ordinary chondrites we use a density of 3.5 g/cm^3. The matrix effect for metal-rich meteorites, e.g., stony-iron meteorites and pallasites, will be discussed in a separate paper. As already demonstrated by Kollàr (2004) and Kollàr et al. (2006) the matrix effect for H, L, and LL chondrites is limited to thermal neutrons, it is almost negligible for protons or for neutrons with higher than thermal energies. As a conclusion from this modeling, it is possible to give elemental production rates valid for all types of ordinary chondrites. The only exceptions are cosmogenic nuclides produced by thermal neutron captures, for which a matrix effect exists. Consequently, the production rates for the only thermal neutron capture reaction considered in this study, i.e., ^{129}I production from Te, are strictly valid only for L chondrites. However, the differences between H, L, and LL chondrites are small (Kollàr 2004; Kollàr et al. 2006) and are neglected in this study.

In contrast to the very similar elemental production rates for the different types of ordinary chondrites, there is a significant matrix effect for ordinary (OC) and carbonaceous chondrites (CC), which is due to the fact that the production of secondary particles and especially neutrons is lower in CCs than in OCs due to the lower Fe content of the former. As a consequence, the neutron flux densities in CCs are, at the same depth in (g/cm^2), more than a factor of 7 lower than in OCs (Fig. 12). In addition, the higher H content in CCs than in OCs results in significant thermal neutron fluxes already in CCs with radii of about 20 cm. In contrast, in OCs thermal neutrons become important only for objects with radii larger than about 50 cm. In Fig. 12a, we show that a significant matrix effect between OCs and CCs only exists for thermal and epithermal neutrons; any differences in the particle spectra and flux densities for protons are negligible (the observed differences at large shielding depths are due to statistical scatter). Consequently, when comparing production rates in OCs and CCs we expect a matrix effect only for those products that are dominantly been produced by secondary neutrons. As an example we show in Fig. 12b for OCs and CCs the ^{21}Ne production rates at the center as a function of radius (in g/cm^2). The production rates in CCs are higher than in OCs. The differences vary with object size from ~10% for small chondrites to ~30% for objects larger than ~700 g/cm^2, i.e., for L and C chondrites with radii of ~200 and ~300 cm, respectively. Panels c and d of Fig. 12 demonstrate that the matrix effect can also be seen for some depth profiles, e.g., for the production of ^{21}Ne and ^{38}Ar from Mg and Ca, respectively. In both panels we compare the depth profiles for L chondrites with radii of 20 cm (70 g/cm^2) and 35 cm (122.5 g/cm^2) with those for C chondrites with radii of 30 cm (67.5 g/cm^2) and 50 cm (112.5 g/cm^2). Both plots demonstrate that the differences increase with increasing shielding, indicating that the production of secondary neutrons and their moderation is the dominant (only) matrix effect.

In Table 3, we compare the matrix effect modeled here

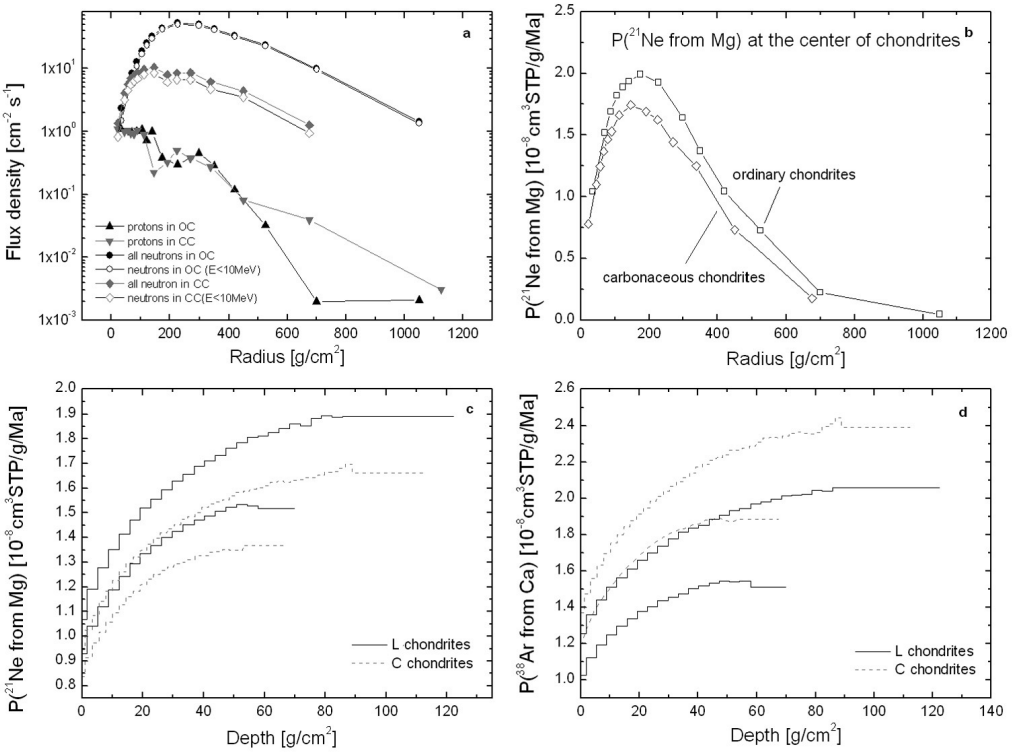

Fig. 12. The matrix effect for ordinary (OC) and carbonaceous chondrites (CC). Panel a shows flux densities for protons, neutrons, and low energy neutrons (E < 10 MeV) at the center of OCs and CCs with radii up to 1100 g/cm^2. Panel b depicts the production rates of ^{21}Ne from Mg at the center of OCs and CCs. Panels c and d show depth profiles for the production of ^{21}Ne from Mg and ^{38}Ar from Ca for OCs with radii of 20 cm and 35 cm and for CCs with radii of 30 cm and 50 cm, respectively.

for some important target product combinations with those calculated earlier by Masarik and Reedy (1994). The following discussion is limited to data from a shielding depth of ~60 g/cm^2 in a chondrite with a radius of ~100 g/cm^2. Note that the predictions by Masarik and Reedy (1994) are based essentially on the same type of model calculations but they used different types of particle spectra and different sets of excitation functions. The data indicate that both approaches agree in that they predict no, or only a very minor, matrix effect for the production of high to medium energy cosmogenic nuclides, i.e., ^{10}Be from O, Si, Fe, ^{14}C from O, Si, Fe, ^{21}Ne from Al, Si, ^{22}Ne from Si, ^{26}Al from Fe, ^{36}Cl from Ti, Fe, and ^{38}Ar from Ca, Fe. For nuclides affected by the matrix effect, our estimates of them are generally lower than the predictions by Masarik and Reedy (1994). For example, while the latter authors predict that ^{38}Ar production from Ca is 15% higher in L chondrites compared to C chondrites our new data predict differences of only 3%. For the production of ^{26}Al from Si we predict 3% higher production rates in L chondrites relative to C chondrites, whereas Masarik and Reedy (1994) modeled a matrix effect of about 7%. Large differences also exist for the production of ^{22}Ne from Mg and Al. While the earlier study modeled a matrix effect of 14% and 15%, respectively, our new data suggest differences of only 4% for both target product combinations. In contrast to these discrepancies, both models predict very similar matrix effects for the production of ^{21}Ne from Mg (8–10%) and ^{53}Mn from Fe (4–7%).

To summarize, considering OCs and CCs the model predicts a significant matrix effect only for nuclides produced dominantly by low energy neutrons. For such nuclides effects of up to 30% are possible, i.e., we model up to 30% higher ^{21}Ne production from Mg in CCs than in OCs. For most of the other target product combinations the differences are either negligible or only within a few percent.

SHIELDING CONDITIONS, EXPOSURE AGES, TERRESTRIAL AGES, AND DIFFUSIVE LOSSES

In the following sections we discuss some elemental and isotopic production rate ratios useful for the study of shielding conditions, i.e., meteoroid size and sample depth, cosmic-ray exposure ages, terrestrial ages, and diffusive losses.

Shielding conditions: For reasons not yet understood, the new model predictions for the shielding indicator ^{22}Ne/^{21}Ne are slightly too high (a few percent) compared to the experimental data. We therefore adjusted the modeled ratios by a size and depth dependent factor, which has been determined by comparing measured and modeled ^{22}Ne/^{21}Ne depth profiles for ALHA78084, Keyes, Knyahinya, and St.

Table 3. Elemental production rates [atoms/min/kg-element] for some cosmogenic nuclides from their major target elements. The calculations are for a depth of about 60 g/cm^2 in a meteoroid with a radius of about 100 g/cm^2.

	Target	Masarik and Reedy (1994)		This	
Nuclide	element	C chondrites	L chondrites	C chondrites	L chondrites
^{10}Be	O	39.5	40.2	43.7	43.5
	Si	8.6	8.6	8.3	8.4
	Fe	4.9	4.8	4.3	4.3
^{14}C	O	103	106	151	157
	Si	14.1	14.1	11.2	11.1
	Fe	4.0	4.0	2.97	3.01
^{21}Ne	Mg	754	820	817	880
	Al	276	280	370	368
	Si	174	178	260	258
^{22}Ne	Mg	827	945	903	939
	Al	341	394	467	475
	Si	206	236	303	302
^{26}Al	Al	724	780	512	546
	Si	268	287	311	320
	Fe	3.1	3.1	3.6	3.7
^{36}Cl	Ca	218	250	204	210
	Ti	58	58	68.5	68.6
	Fe	22.5	22.7	23.8	23.7
^{38}Ar	Ca	1354	1436	1164	1210
	Fe	47	49	33.6	34.2
^{53}Mn	Fe	439	471	533	551

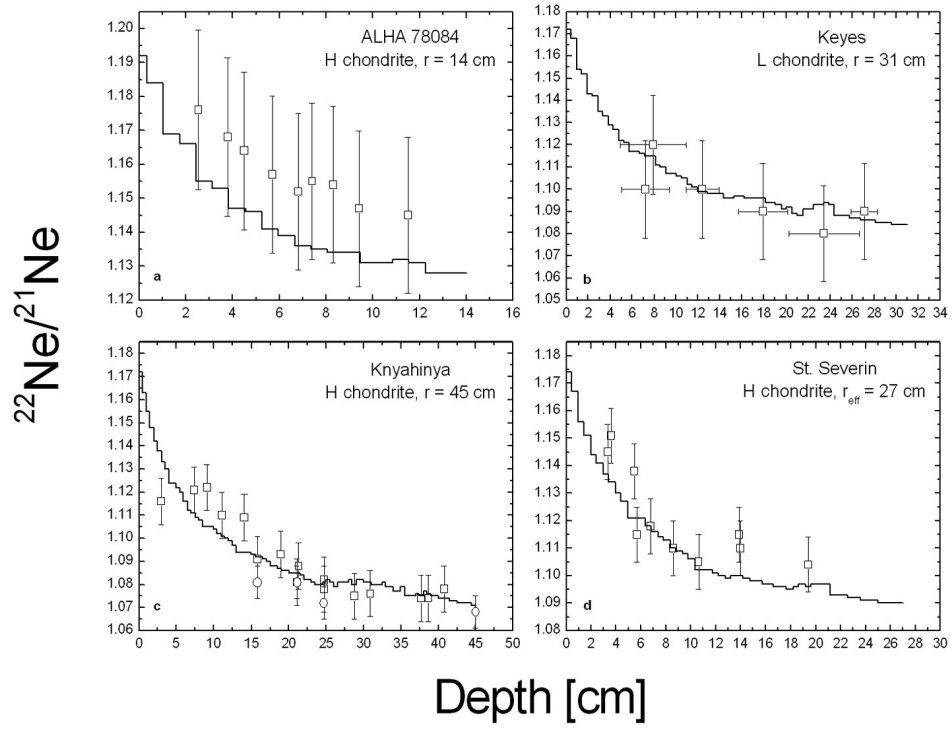

Fig. 13. Calculated and measured ^{22}Ne/^{21}Ne depth profiles for ALHA 89084, Keyes, Knyahinya, and St.Severin. The experimental data are from Sarafin (1985), Cressy (1975), and Schultz and Signer (1976). Shown are the ^{22}Ne/^{21}Ne ratios after the adjustment (see text).

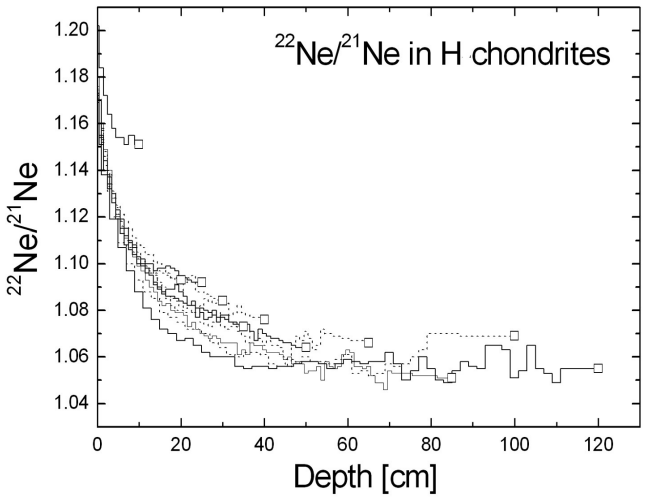

Fig. 14. Calculated depth profiles for $^{22}Ne/^{21}Ne$ in H chondrites with radii between 5 and 120 cm. Shown are the $^{22}Ne/^{21}Ne$ ratios after the adjustment (see text).

Severin. After this adjustment the model is able to accurately reproduce $^{22}Ne/^{21}Ne$ ratios (Fig. 13)—at least for the four meteorites shown here. The model predictions for $^{22}Ne/^{21}Ne$ are no longer purely physical but are slightly adjusted by an empirical factor, which is given in the Excel-Sheet and which varies between 0.98 for small meteorites and ~0.90 for high shielding depths in large objects. We are unable to adjust the model predictions for carbonaceous chondrites (we do not even know if an adjustment is necessary) due to the lack of measured $^{22}Ne/^{21}Ne$ depth profiles. Figure 14 shows $^{22}Ne/^{21}Ne$ ratios (after adjustment) for H chondrites with radii between 10 cm and 120 cm. With these data and having in mind that $^{22}Ne/^{21}Ne$ ratios are usually measured with an uncertainty of about 1%, it becomes obvious that the shielding indicator can reliably be used only for objects with radii smaller than ~60 cm.

For the target element Mg, the model predicts—without any adjustments—$^{22}Ne/^{21}Ne$ ratios between 1.04 and 1.21 with an average ratio of 1.07 (considering all shielding depths in objects with radii less than 120 cm). At first glance, the model seems to contradict experimental data from Begemann et al. (1976), who include $^{22}Ne/^{21}Ne$ ratios from Mg lower than unity for stony-iron meteorites. However, this (obvious) discrepancy is due to the matrix effect. The $^{22}Ne/^{21}Ne$ ratios from Mg in iron meteorites (Ammon et al. 2008a) vary between 0.93 and 1.3, with an average ratio of 0.99, which is indeed slightly lower than unity. The $^{22}Ne/^{21}Ne$ ratios from Mg for carbonaceous chondrites vary between 0.99 and 1.32, with an average ratio of 1.12, again indicating the influence of the matrix effect.

Since $^{22}Ne/^{21}Ne$ ratios cannot be used as shielding indicators for large objects we propose the relationship between ^{10}Be in bulk samples versus ^{10}Be in metal separates as a reliable proxy for meteoroid sizes and shielding depths. For the same purpose ^{26}Al can also be used. The model predictions for both nuclides are shown in Fig. 15. Similar plots have already been used to determine the preatmospheric radii of large chondrites, e.g., Gold Basin (Welten et al. 2003) and JaH 073 (Huber et al. 2008).

Exposure ages: Very popular for the determination of cosmic-ray exposure ages is the ^{21}Ne–$^{22}Ne/^{21}Ne$ method. Most studies use the empirical correlations given by Nishiizumi et al. (1980) or Eugster (1988). Both correlations are compared to our new model predictions in Fig. 16. Two major results are of importance. First, it can be seen that our model predictions confirm both empirical correlations at low shielding, i.e., high $^{22}Ne/^{21}Ne$, and second, the model demonstrates that the correlation between ^{21}Ne production rates and $^{22}Ne/^{21}Ne$ ratios is ambiguous for large objects, as has been known for some time. The latter is due to the fact that for large shielding depths $^{22}Ne/^{21}Ne$ ratios show only minor variations (or even starts to increase with shielding) while the ^{21}Ne production rates continue to decrease with increasing shielding. This becomes obvious already for objects with radii larger than ~65 cm (Fig. 16). Consequently, with this relationship a reliable age can only be obtained for objects smaller than that. For them we can give a best fit line for the individual model predictions:

$$P(^{21}Ne) = F \times \{2.22 - 1.71 \times (^{22}Ne/^{21}Ne)\} [10^{-8} cm^3 STP/g/Ma] \quad (2)$$

with $P(^{21}Ne)$ the production rate [10^{-8}cm^{3}STP/g/Ma] and F = 1.00, 1.07, and 1.09 for H, L, and LL chondrites, respectively. This simple correlation, which is also shown in Fig. 16, is only valid for meteorites with radii less than about 65 cm. The cosmic-ray exposure ages determined via Equation 2 for Knyahinya, Keyes, Bansur, ALHA78084, Udaipur, and St. Severin are given in Table 2.

Due to the limitations of the ^{21}Ne–$^{22}Ne/^{21}Ne$ method for large meteorites, we have to search for a new system to determine cosmic-ray exposure ages for them. Here we propose an improved version of the ^{10}Be–^{21}Ne and ^{26}Al-^{21}Ne methods. Plotting modeled $^{21}Ne/^{10}Be$ ratios in bulk samples as a function of ^{10}Be in metal aliquots yields an unambiguous correlation, which holds for all meteoroids with radii less than about 300 cm, i.e., for almost all meteoroid sizes occurring in nature (Fig. 17, left panel). The right panel of Fig. 17 demonstrates that the same method also works if one uses $^{26}Al/^{21}Ne$ instead of $^{21}Ne/^{10}Be$. Both correlations can be fitted using a functional of the form:

$$^{21}Ne/(^{10}Be, ^{26}Al) = a \times (^{10}Be \text{ in metal})^{-b} \quad (3)$$

with $^{21}Ne/^{10}Be$ and/or $^{21}Ne/^{26}Al$ measured in bulk samples [10^{-8}cm^{3}STP/g/Ma per dpm/kg] and ^{10}Be in metal aliquots [dpm/kg]. The fit-parameters *a* and *b* for both systems are given together with the reduced χ^2-value in Table 4.

Another reliable system for the determination of cosmic-ray exposure ages is the ^{36}Cl-^{36}Ar method, which is

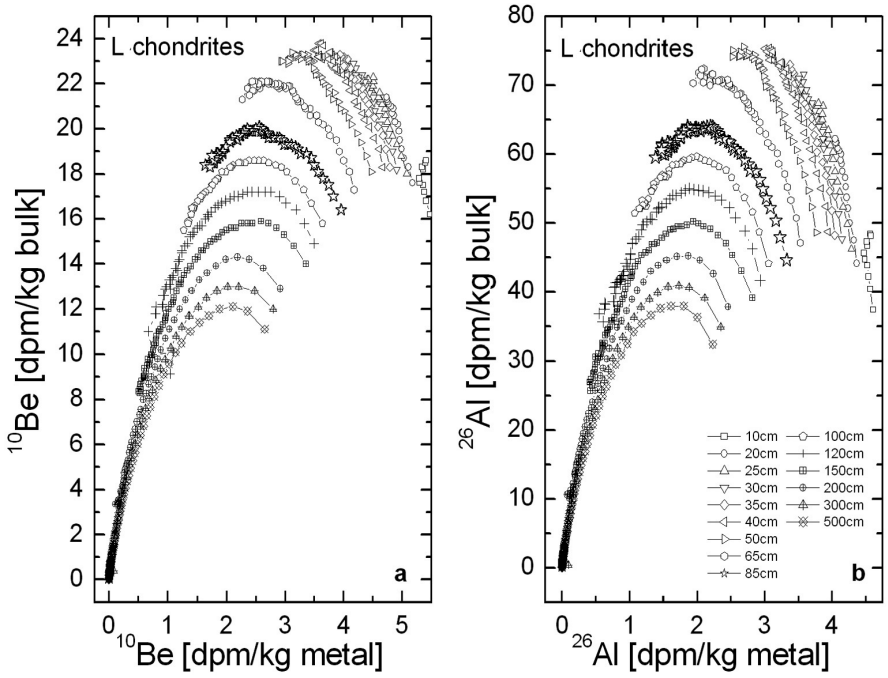

Fig. 15. ^{10}Be in bulk samples as a function of ^{10}Be measured in metal separates (panel a) and ^{26}Al in bulk samples as a function of ^{10}Be measured in metal separates (panel b). Both plots enable (at least roughly and for large objects) to determine the preatmospheric size of the meteorite.

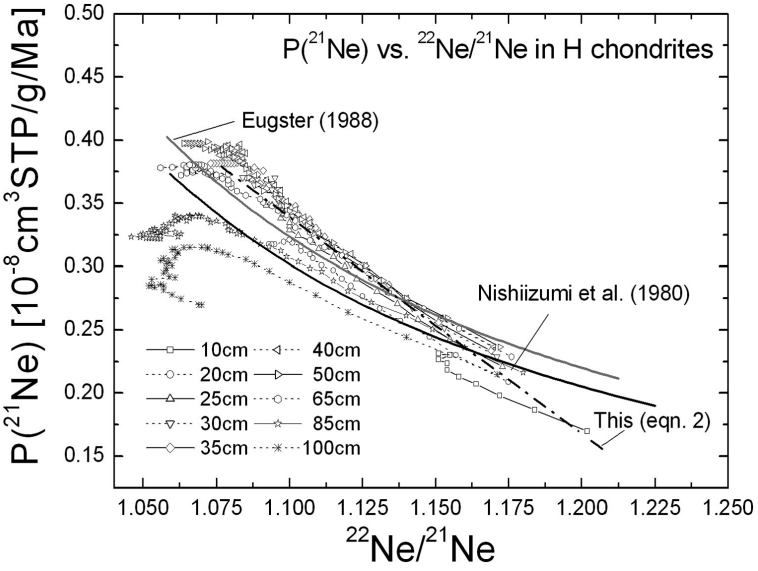

Fig. 16. Modeled ^{21}Ne production rates versus ^{22}Ne/^{21}Ne for H chondrites with radii between 10 cm and 100 cm. The model predictions for R < 65 cm agree reasonably well with the empirical correlations given by Nishiizumi et al. (1980) and Eugster (1988).

especially reliable because in the metal phase of ordinary chondrites—as well as in iron meteorites and the metal phase of other meteorite types—most ^{36}Ar is produced via the radioactive decay of ^{36}Cl (see also above). Hence, ^{36}Ar production rates can unambiguously be determined from measured ^{36}Cl concentrations via:

$$P(^{36}\mathrm{Ar}) = 2.28 \times 10^{-3} \times P(^{36}\mathrm{Cl}) \quad (4)$$

with P(^{36}Ar) and P(^{36}Cl) are in [10^{-8}cm^{3}STP/gFe/Ma] and [dpm/kgFe], respectively. The factor 2.28×10^{-3} is due to the unit conversion between dpm/kg and cm^{3}STP/g/Ma and included the branching ratio. This relation is in good agreement with the ^{36}Cl/^{36}Ar production rate ratio given by Graf et al. (2001) and Lavielle et al. (1999) but yields about 3% higher ^{36}Ar production rates than the relationship given by Begemann et al. (1976). Using measured ^{36}Ar

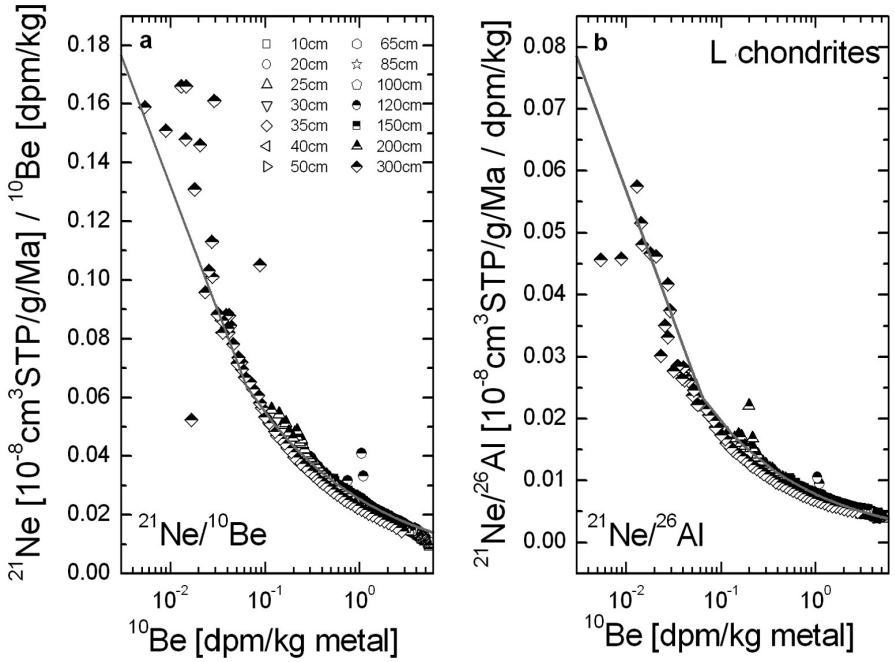

Fig 17. ^{21}Ne/^{10}Be versus ^{10}Be(metal) (left panel) and ^{21}Ne/^{26}Al versus ^{10}Be(metal) (right panel) for L chondrites with radii between 10 cm and 300 cm. The symbols indicate the individual model predictions for all shielding depths and radii, the solid grey lines are bests fits through the model predictions (see text). Both correlations enable a precise and size independent calculation of cosmic-ray exposure ages.

concentrations [10^{-8}cm^{3}STP/g] and the ^{36}Cl production rates [dpm/kg] the cosmic-ray exposure age T_{irr} [Ma] can be calculated via:

$$T_{irr} = 438.6 \times \frac{cc(^{36}\mathrm{Ar})}{P(^{36}\mathrm{Cl})} + 3.65 \times 10^{-2} \qquad (5)$$

where the additional constant takes into account that some ^{36}Cl, those actually measured as ^{36}Cl and has not yet decayed to ^{36}Ar. As expected, the additional constant is important only for very low exposure ages. We consider as an example a meteorite with an exposure age of 2 Ma. Neglecting that some ^{36}Cl has not yet decayed to ^{36}Ar results in an age too low by about 2%. For an age of 7 Ma the error is only 0.5%, i.e., negligible compare to the other uncertainties involved.

Cosmogenic ^{4}He/^{3}He ratios: Fig. 18 shows modeled cosmogenic ^{4}He/^{3}He ratios in H chondrites with radii between 10 cm and 120 cm. The model predictions of ~3.5 for small and ~6 for large meteoroids are smaller than the ratio of 6.2 ± 0.2 (Welten et al. 2003) or 6.1 ± 0.3 (Alexeev 1998) used so far for chondrites. If one considers only meteoroids with radii less than 120 cm and only the innermost 20%, i.e., if we assume a mean ablation loss of about 80%, the mean cosmogenic ^{4}He/^{3}He ratio is 5.6 ± 0.5, which is still lower than the values preferred by Alexeev (1998) and Welten et al. (2003) but is in agreement with the ratio assumed by Begemann et al. (1976). To better constrain the cosmogenic ^{4}He/^{3}He ratios we plotted them as a function of ^{22}Ne/^{21}Ne (Fig. 18b) and obtained a linear dependency:

$$^4\mathrm{He}/_3\mathrm{He} = (25.7 \pm 0.2) - (18.6 \pm 0.2) \times \left(^{22}\mathrm{Ne}/_{21}\mathrm{Ne}\right) \qquad (6)$$

Diffusive losses of ^{3}H/^{3}He: Diffusive losses of radioactive ^{3}H or of the daughter element ^{3}He are often used to get information about the thermal history of meteorites. Graf et al. (2001) have shown in a systematic study of H chondrites that ^{3}H loss from metal is, at least for falls of the 7 Ma exposure age peak, significantly more frequent among the H5 than H4 falls, consistent with the interpretation that a subgroup of the H chondrites experienced a distinct orbital evolution. Usually ^{3}H/^{3}He diffusive losses are discussed using the Bern plot, i.e., the diagram of ^{3}He/^{21}Ne versus ^{22}Ne/^{21}Ne. Our model predictions for the Bern plot are shown in Fig. 19, where the symbols connected by lines indicate the individual modeled results for H chondrites with radii between 10 and 100 cm. The solid grey line indicates the empirical correlation given by Eugster (1988), which differs only slightly from the original one proposed by Eberhardt et al. (1966). The solid black line is a best fit through our model predictions, assuming an ablation loss of about 80%, i.e., considering only the innermost 20% of the meteoroid. It can be seen that the model predicts significantly higher ^{3}He/^{21}Ne ratios—at the same ^{22}Ne/^{21}Ne—than the empirical correlation. For example, at ^{22}Ne/^{21}Ne = 1.125 our new correlation is about 15% higher than the so far used empirical approach. Whether this discrepancy indicate that *i*) most of the meteorites lost some He (especially those used by Eugster (1988) to determine the correlation) or *ii*) whether it might be

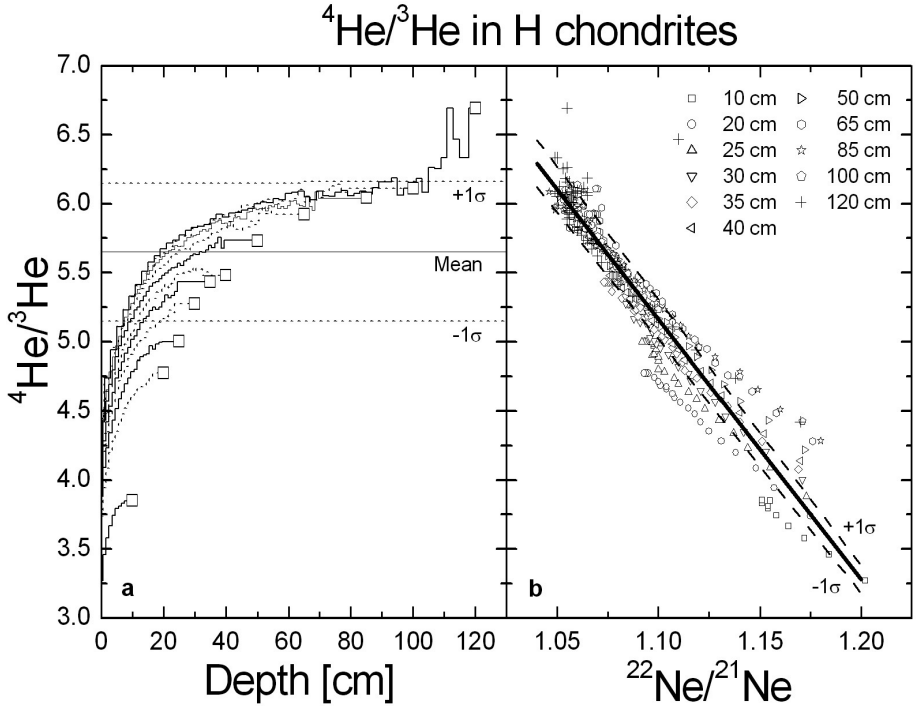

Fig. 18. Cosmogenic $^4He/^3He$ depth profiles for H chondrites with radii between 5 cm and 120 cm (panel a) and $^4He/^3He$ ratios as a function of $^{22}Ne/^{21}Ne$ (panel b). Most of the cosmogenic $^4He/^3He$ ratios are lower than the ratios of 6.2 ± 0.2 and 6.1 ± 0.3 given by Welten et al. (2003) and Alexeev (1998) assumed so far. Considering only the innermost 20%, i.e., assuming 80% ablation losses, results in an average modelled $^4He/^3He$ ratio of 5.6 ± 0.5 shown by the solid black line. The dotted lines are the ±1σ standard deviations of the mean.

Table 4. Fit parameter and reduced χ^2 values for the $^{21}Ne/^{10}Be$(bulk) versus ^{10}Be(metal) and $^{21}Ne/^{26}Al$(bulk) versus ^{10}Be(metal) systems to determine cosmic-ray exposure ages in large ordinary chondrites.

	$^{21}Ne/^{10}Be$(bulk)-^{10}Be(metal) system		
Type of meteorite	Parameter a	Parameter b	χ^2
H chondrites	0.03076	–0.33717	0.00028
L chondrites	0.02542	–0.33366	0.00019
LL chondrites	0.02973	–0.33611	0.00026
	$^{21}Ne/^{26}Al$(bulk)-^{10}Be(metal)		
Type of meteorite	Parameter a	Parameter b	χ^2
H chondrites	0.00934	–0.40326	2.29×10^{-6}
L chondrites	0.00783	–0.39698	1.75×10^{-6}
LL chondrites	0.00926	–0.40311	2.25×10^{-6}

due to the fact that ablation is usually not symmetric and that we therefore cannot directly compare measured data and model predictions is not yet clear and further studies are needed. The model also predicts considerable scatter around the correlation line. This scatter can also be seen in the experimental data. We therefore also plotted in Fig. 19 measured data for St. Severin, which confirm the model predictions in that they are higher than the empirical correlation by Eugster (1988). The Bern plot is not useful for very large meteoroids, i.e., for objects in the size range of a few meters. This limitation is due to the fact that for large objects the correlation between $^3He/^{21}Ne$ versus $^{22}Ne/^{21}Ne$ is no longer linear because $^{22}Ne/^{21}Ne$ stays constant or even increases with shielding while $^3He/^{21}Ne$ further decreases (Huber et al. 2008; Welten et al. 2003). Consequently, when discussing ^3H diffusive losses in meteorites one has to be very careful and a proper study should not rely on the $^3He/^{21}Ne$ versus $^{22}Ne/^{21}Ne$ systematic alone.

Tritium and ^3He diffusive losses can also be illustrated plotting $^3He/^{38}Ar$(metal) as a function of ^3He(stone)/^{38}Ar(metal) (Fig. 20, see also Begemann et al. [1976]). For the following discussion we consider only meteorites with radii between 10 cm and 120 cm: the ranges given for the elemental ratios are due to size and shielding effects. For metal samples without diffusive losses, the $^3He/^{38}Ar$ ratio varies between 16.4 and 18.6 with an average of 17.5. For ^3He(stone)/^{38}Ar(metal) the model predicts ratios between ~30 and ~48 with an average of ~39. Total ^3H diffusive losses in metal and silicates result in average $^3He/^{38}Ar$(metal) and ^3He(stone)/^{38}Ar(metal) ratios of 6.5 and 18.6, respectively. The sizes of the ellipsoids shown in Fig. 20 are given by the standard deviations of the mean values. Samples without diffusive losses in metal and silicates plot within the upper right ellipsoid. While losing ^3H from the metal the data move along the line towards the lower right ellipsoid. Note that most samples are expected to move along this line because it has often been shown that ^3H diffusive losses in metal are much

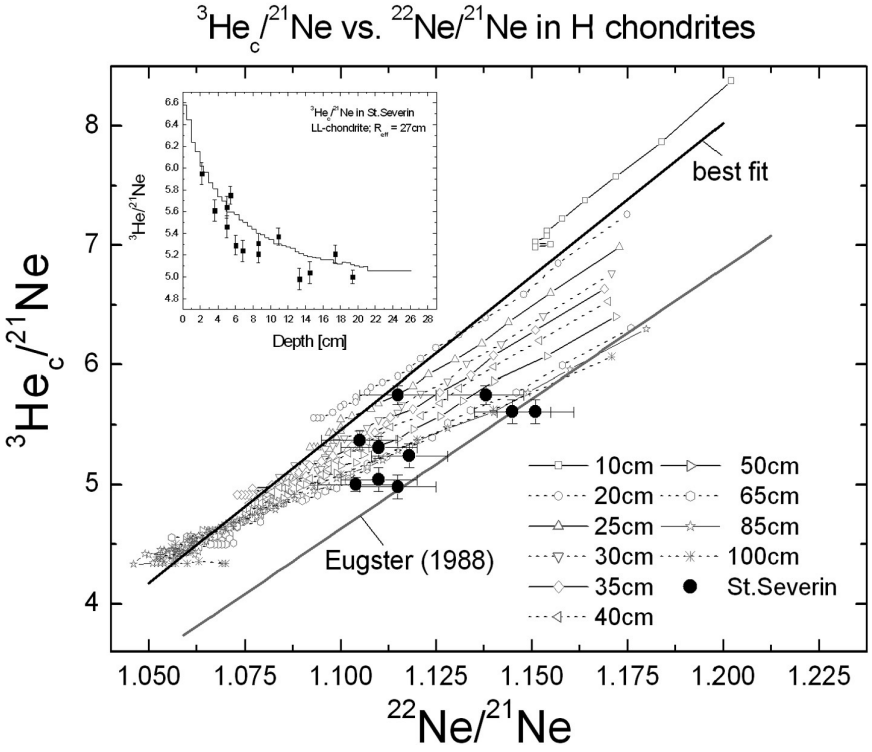

Fig. 19. $^3He/^{21}Ne$ as a function of $^{22}Ne/^{21}Ne$ for H chondrites. The grey symbols (connected either by solid or dotted lines) indicate the results of the model calculations for H chondrites with radii between 10 cm and 100 cm. The grey solid line is the empirical correlation given by Eugster (1988), which differ only slightly from the original correlation proposed by Eberhardt et al. (1966). The black solid line is the best fit through the model calculations, assuming about 80% ablation loss. Also shown are experimental data for St. Severin, which confirm the new model predictions in that they are higher than the empirical correlation and show some scatter.

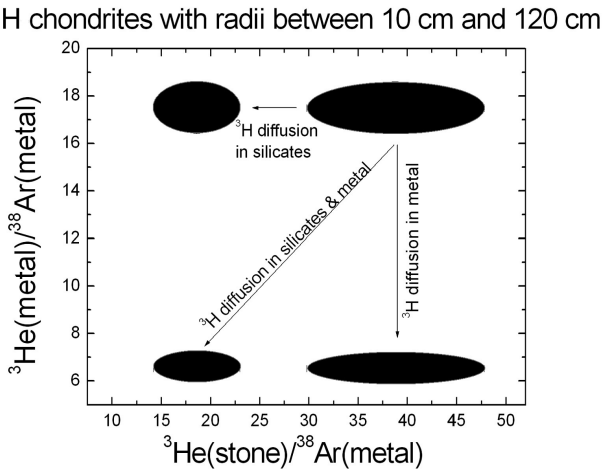

Fig. 20. $^3He/^{38}Ar$(metal) versus ^3He(stone)/^{38}Ar(metal) in H chondrites with radii between 10 cm and 120 cm. The position of the ellipsoids are given by the average values of the model calculations assuming 80% ablation loss. The sizes of the ellipsoids are given by the standard deviations of the means. Samples without ^3H and/or ^3He diffusive losses plot in the upper right of the diagram. Samples loosing only ^3H and/or ^3He from the metal move towards the lower right of the diagram. Samples loosing only ^3H and/or ^3He from silicate move to the upper left and samples loosing ^3H and/or ^3He from both, metal and silicates, move to the lower left. From this diagram diffusive losses can easily be quantified.

more pronounced than in silicate minerals (e.g., Hintenberger et al. 1966; Leya et al. 2001b). Samples loosing only ^3H and/or ^3He from the silicates move from the upper right to the upper left and samples losing ^3H and/or ^3He in both, metal and silicates, move towards the lower left ellipsoid. Consequently, from the position of the sample within this diagram one can quantify ^3H and/or ^3He diffusive losses in metal and silicate minerals.

SUMMARY AND CONCLUSION

We present a purely physical model for the calculation of depth and size dependent cosmogenic production rates in ordinary and carbonaceous chondrites with radii between 10 cm and 500 cm. The model is based on our current best knowledge of the particle spectra and the relevant nuclear reactions and therefore replaces of our earlier calculations (Leya et al. 2000a). The new modeling describes production rates for most cosmogenic radionuclides within their uncertainties, which are within 10–15%. One exception is ^{14}C, for which the model overestimates the experimental data by ~40%. The reason for this shortcoming is not yet understood. Systematic discrepancies between modeled and experimental production rates also exist for ^{53}Mn, which are due to the fact that all input data used for modeling were

measured by AMS, while the meteorite data were measured by neutron activation techniques. The 29% offset between modeled and measured data is most probably due to the different standards used in the different setups.

Along with the elemental production rates for radionuclides we also present a reliable and consistent database for cosmogenic production rates of ^{3}He, ^{4}He, ^{20}Ne, ^{21}Ne, ^{22}Ne, ^{36}Ar, and ^{38}Ar from the major target elements. The input data used for modeling ^{3}He are corrected for ^{3}H diffusive losses during irradiation and/or storage and they are based on our current best knowledge of the ^{3}H/^{3}He branching ratios, making this the first version of model calculations able to accurately predict ^{3}He production rates. Whenever possible, we compared modeled production rates and production rate ratios to experimental data and found in most cases good agreements.

Based on the new model predictions, we present some elemental and isotopic ratios for the determination of shielding conditions, exposure ages, and diffusive losses. The modeled ^{22}Ne/^{21}Ne ratios, for which a slight adjustment was necessary, demonstrate that this shielding indicator is reliable only for objects with radii <65cm. For larger chondrites, we propose relations of the type ^{10}Be(bulk) versus ^{10}Be(metal) and/or ^{26}Al(bulk) versus ^{26}Al(metal) for the determination of preatmospheric sizes. Cosmic-ray exposure ages are often determined via the ^{21}Ne-^{22}Ne/^{21}Ne method, which we show is not reliable for large objects. For smaller meteorites the model predictions agree reasonably well with the empirical correlations used so far, e.g., Nishiizumi et al. (1980) and Eugster (1988). For larger objects we propose relationships of the form ^{21}Ne/^{10}Be(bulk) versus ^{10}Be(metal) and/or ^{21}Ne/^{26}Al(bulk) versus ^{10}Be(metal) as possible exposure age proxies. Both systems enable a reliable determination of cosmic-ray exposure ages for all meteorite sizes and shielding depths.

The new model is the first version able to accurately predict cosmogenic production rates for ^{3}He and ^{4}He. Reliable modeling of ^{3}He is now possible thanks to our recent study of ^{3}H diffusive losses in irradiation experiments (Leya et al. 2004a, 2008) and some recent data for the ^{3}H/^{3}He branching ratios (Herbach et al. 2006). Modeling ^{4}He is now especially reliable thanks to our recent cross section study (Ammon et al. 2008b). Based on this new input data we model an average cosmogenic ^{4}He/^{3}He ratio of ~5.5, which is slightly lower but comparable to the values of 6.2 ± 0.2 and 6.1 ± 0.3 given by Welten et al. (2003) and Alexeev (1998). In addition we propose a linear correlation between ^{4}He/^{3}He and ^{22}Ne/^{21}Ne, which enable a reliable estimate of cosmogenic ^{4}He/^{3}He ratios. This in turn may allow better delineation of solar or radiogenic ^{4}He contributions.

We also discuss the model predictions for ^{3}He/^{21}Ne versus ^{22}Ne/^{21}Ne, i.e., the Bern plot. The modeled correlation is about 15% higher than the empirical approach used so far (e.g., Eberhardt et al. 1966; Nishiizumi et al. 1980) but agrees with measured St. Severin data (Schultz and Signer 1976) within the experimental uncertainties. The model indicates that the scatter around the correlation line is substantial, which significantly limits its applicability to detect small ^{3}H and/or ^{3}He diffusive losses. To better quantify such losses we presented a diagram ^{3}He/^{38}Ar(metal) versus ^{3}He(bulk)/^{38}Ar(metal), which enable to study ^{3}He and/or ^{3}He diffusive losses in meteoritic metal and silicate phases in some detail.

Finally, in addition to the data for ordinary chondrites, for the first time we also present here a comprehensive data set for cosmogenic nuclide production rates in carbonaceous chondrites. If the size and depth scale is discussed in g/cm^{2}, the only relevant matrix effect, at least for ordinary and carbonaceous chondrites, is for reactions induced by thermal and very low energy neutrons. As an example, for the production of ^{21}Ne from Mg the matrix effect is up to 30%. For all other target product combinations, the matrix effect for both chondrite types is very small and can be neglected considering the other uncertainties involved in modeling cosmogenic nuclide production rates.

Editorial Handling—Dr. Marc Caffee

REFERENCES

Alexeev V. A. 1998. Parent bodies of L and H chondrites: Times of catastrophic events. *Meteoritics & Planetary Science* 33:145–152.

Ammon K., Masarik J., and Leya I. 2008a. New model calculations for the production rates of cosmogenic nuclides in iron meteorites. *Meteoritics & Planetary Science* 44:485–503.

Ammon K., Leya I., Lavielle B., Gilabert E., David J.-C., Herpers U., and Michel R. 2008b. Cross sections for the production of helium, neon, and argon isotopes by proton-induced reactions on iron and nickel. *Nuclear Instruments and Methods in Physics Research B* 266:2–21.

Armstrong T. W. and Chandler K.C. 1972. HETC—A high energy transport code. *Nuclear Science Engineering* 49:110.

Aylmer D., Bonanno V., Herzog G. H., Weber H., Klein J., and Middleton R. 1988. ^{26}Al and ^{10}Be production in iron meteorites. *Earth and Planetary Science Letters* 88:107–118.

Arnold J. R., Honda M., and Lal D. 1961. Record of cosmic-ray intensity in the meteorites. *Journal of Geophysical Research* 66: 3519–3539.

Begemann F., Weber H. W., Vicsek E., and Hintenberger H. 1976. Rare gases and ^{36}Cl in stony iron meteorites: Cosmogenic elemental production rates, exposure ages, diffusion losses, and thermal histories. *Geochimica et Cosmochimica Acta* 40:353–368.

Begemann F. and Schultz L. 1988. The influence of bulk chemical composition on the production rate of cosmogenic nuclides in meteorites (abstract). 19th Lunar and Planetary Science Conference. pp. 51–52.

Bhattacharya S. K., Imamura M., Sinha N., and Bhandari N. 1980. Depth and size dependence of ^{53}Mn activity in chondrites. *Earth and Planetary Science Letters* 51:45–57.

Bochsler P., Eberhardt P., Geiss J., and Grögler N. 1969. Rare-gas measurements in separate mineral phases of the Otis and

Elenovka chondrites. In *Meteorite research*, edited by P. Millman. Berlin: Springer. pp. 857–874.

Bogard D. D. and Cressy P. J. 1973. Spallation production of ^{3}He, ^{21}Ne, and ^{38}Ar from target elements in the Bruderheim chondrite. *Geochimica et Cosmochimica Acta* 37:527–546.

Boudard A., Cugnon J., Leray S., and Volant C. 2002. Intranuclear cascade model for a comprehensive description of spallation reaction data. *Physical Review C* 66:044615.

Broeders C. H. M., Konobeyev A. Yu., and Mercatali L. 2006. Global comparison of TALYS and ALICE code calculations and evaluated data from ENDF/B, JENDL, and JEFF Files with measured neutron induced reaction cross sections at energies above 0.1 MeV. *Journal of Nuclear and Radiochemical Sciences* 7(1):N1–N4.

Carpenter J. M. 1987. Pulsed spallation neutron sources for slow neutron scattering. *Nuclear Instruments and Methods* 145:91–113.

Cloth P., Filges D., Neef R. D., Sterzenbach G., Reul Ch., Armstrong T. W., Colborn B. L., Anders B., and Brückmann H. 1988. HERMES—High Energy Radiation Monte-Carlo Elaborate System. JUEL-2203.

Cressy P. J. 1975. Aluminum-26 in cores of the Keyes chondrite. *Journal of Geophysical Research* 80:1551–1553.

Duijvestijn M. and Koning A. J. 2006. New intermediate-energy nuclear data libraries for Fe. *Annals of Nuclear Energy* 33:1196–1226.

Eberhardt P., Eugster O., Geiss J., and Marti K. 1966. Rare gas measurements in 30 stone meteorites. *Zeitschrift für Naturforschung Teil A* 21:414–426.

Emmett M. B. 1975. The MORSE Monte Carlo Radiation Code System. ORNL-4942, Oak Ridge, Tennessee, USA.

Englert P. and Herr W. 1980. On the depth-dependent production of long-lived spallogenic ^{53}Mn in the St. Severin chondrite. *Earth and Planetary Science Letters* 47:361–369.

Eugster O. 1988. Cosmic-ray production rates for He-3, Ne-21, Ar-38, Kr-83, and Xe-126 in chondrites based on Kr-Kr-81 exposure ages. *Geochimica et Cosmochimica Acta* 52:1649–1662.

Eugster O., Herzog G. F., Marti K., and Caffee M. W. 2006. Irradiation records, cosmic-ray exposure ages, and transfer times of meteorites. In *Meteorites and the early solar system*, edited by Lauretta D. S. and McSween H. Y. Jr. Tucson: The University of Arizona Press. pp. 829–851.

Eugster O., Lorenzetti S., Krähenbühl U., and Marti K. 2007. Comparison of cosmic-ray exposure ages and trapped noble gases in chondrule and matrix samples of ordinary, enstatite, and carbonaceous chondrites. *Meteoritics & Planetary Science* 42: 1351–1371.

Feshbach H. 1992. *Theoretical nuclear physics: Nuclear reactions*. John Wiley & Sons. 960 p.

Gopalan K. and Rao M. N. 1976. Rare gases in Bansur, Udaipur and Madhipura chondrites. *Meteoritics* 11:131–136.

Goswami J. N. 1983. Nuclear track records in the Abee enstatite chondrite. *Earth and Planetary Science Letters* 62:159–164.

Graf Th. 1988. Produktion kosmogener Nuklide in Meteorites. Ph.D. thesis, ETH Zürich, Switzerland, 143 p.

Graf Th., Baur H., and Signer P. 1990a. A model for the production of cosmogenic nuclides in chondrites. *Geochimica et Cosmochimica Acta* 44:539–547.

Graf Th., Signer P., Wieler R., Herpers U., Sarafin R., Vogt S., Fleni Ch., Pellas P., Bonani G., Suter M., Wölfli W. 1990b. Cosmogenic nuclides and nuclear tracks in the chondrite Knyahinya. *Geochimica et Cosmochimica Acta* 54:2511–2534.

Graf Th, Caffee M. W., Marti K., Nishiizumi K., and Ponganis K. V. 2001. Dating collisional events: ^{36}Cl-^{36}Ar exposure ages of chondritic metal. *Icarus* 150:181–188.

Herbach C.-M., Hilscher D., Jahnke U., Tishenko V. G., Galin J. G., Letourneau A., Péghaire A., Filges D., Goldenbaum F., Pienkowski L., Schröter W. U., and Toke J. 2006. Systematic investigation of 1.2 GeV proton-induced spallation reactions on targets between Al and U. *Nuclear Instruments and Methods in Physics Research A* 562:729–732.

Herzog G. F. 2005. Cosmic-ray exposure ages of meteorites. In *Meteorites, comets, and planets*, edited by Davis A. M. Treatise on Geochemistry, vol. 1. Amsterdam: Elsevier. p. 347.

Hintenberger H., Schultz L., and Wänke H. 1966. Messung von Diffusionsverlusten von radiogenen und spallogenen Edelgasen in Steinmeteoriten II. *Zeitschrift für Naturforschung Teil A* 21: 1147–1159.

Hintenberger H., Schultz L., Wänke H., and Weber H. 1967. Helium- und Neonisotope in Eisenmeteoriten und der Tritiumverlust in Hexaedriten. *Zeitschrift für Naturforschung Teil A* 22:780–787.

Hofmann H.-J., Beer J., Bonani G., von Gunten R. R., Raman S., Suter M., Walker R. L., Wölfli W., and Zimmermann D. 1987. ^{10}Be: Half-lives and AMS standards. *Nuclear Instruments and Methods in Physics Research B* 29:32–36.

Honda M., Caffee M. W., Miura Y. N., Nagai H., Nagao K., and Nishiizumi K. 2002. Cosmogenic nuclides in the Brenham pallasite. *Meteoritics & Planetary Science* 37:1711–1728.

Huber L., Gnos E., Hofmann B. A., Welten K., Nishiizumi K., Caffee M., Hillegonds D. S., and Leya I. 2008. The complex exposure history of the Jiddat al Harasis 073 L chondrite shower. *Meteoritics & Planetary Science* 43:1691–1708.

Huneke J. C., Podosek F. A., and Wasserburg G. J. 1972. Gas retention and cosmic ray exposure ages of a basalt fragment from Mare Fecunditatis. *Earth and Planetary Science Letters* 13:375–383.

Jarosevich E. 1990. Chemical analyses of meteorites: A compilation of stony and iron meteorite analyses. *Meteoritics* 25:323–337.

Kim K. J., Sisterson J. M., Englert P. A. J., Caffee M. W., Reedy R. C., Vincent J., and Castaneda C. 2002. Experimental cross-sections for the production of ^{10}Be from natural carbon targets with 40.6 to 500 MeV protons. *Nuclear Instruments and Methods in Physics Research B* 196:239–244.

Klein J., Fink D., Middleton R., Vogt S., and Herzog G. F. 1991. ^{41}Ca in the Jilin (H5) chondrite: A matter of size (abstract). *Meteoritics* 26:358.

Knie K., Ebihara M., Faestermann T., Herzog G., Korschinek G., Leya I., Ma P., Oura Y., Rugel G., and Serefiddin F. Forthcoming. Half-life of ^{53}Mn determined by X-ray counting and accelerator mass spectrometry. *Nuclear Instruments and Methods in Physics Research A*.

Kollàr D. 2004. Neutron cross sections and interactions of cosmic ray particles with terrestrial and extraterrestrial matter. Ph.D thesis, Comenius University, Bratislava, Slovakia, 103 p.

Kollàr D., Michel R., and Masarik J. 2006. Monte Carlo simulation of GCR neutron capture production of cosmogenic nuclides in stony meteorites and lunar surface. *Meteoritics & Planetary Science* 41:375–389.

Koning A. J., Hilaire S., and Duijvestijn M. C. 2005. TALYS: comprehensive nuclear reaction modelling. *Proceedings of the International Conference on Nuclear Data for Science and Technology.* pp. 1154–1159.

Lange H.-J. 1994. Über die Wechselwirkung der galaktischen kosmischen Strahlung mit extraterrestrischer Materie. Bestimmung von Dünntargetwirkungsquerschnitten und Modellrechnungen. Ph.D. thesis, University of Hannover, Germany. 257 p.

Lavielle B., Sauvageon H., and Bertin P. 1990. Cross sections for neon and krypton isotopes produced by neutrons. In *Workshop on Cosmogenic Nuclide Production Rates,* edited by Englert P. A. J., Reedy R. C., and Michel R. Houston: Lunar Planetary Institute. pp. 65–69.

Lavielle B., Toè S., and Gilabert E. 1997. Noble gas measurements in the L/LL5 chondrite Knyahinya. *Meteoritics & Planetary Science* 32:97–107.

Lavielle B., Marti K., Jeannot J.-P., Nishiizumi K., and Caffee M. 1999. The ^{36}Cl-^{36}Ar-^{40}K-^{41}K records and cosmic-ray production rates in iron meteorites. *Earth and Planetary Science Letters* 170: 93–104.

Leya I. and Michel R. 1998. Determination of neutron cross sections for nuclide production at intermediate energies by deconvolution of thick-target production rates. *Proceedings of the International Conference on Nuclear Data for Science and Technology.* pp. 1463–1467.

Leya I., Lange H.-J., Neumann S., Wieler R., and Michel R. 2000a. The production of cosmogenic nuclides in stony meteoroids by galactic cosmic-ray particles. *Meteoritics & Planetary Science* 35:259–286.

Leya I., Lange H. J., Lüpke M., Neupert U., Daunke R., Fanenbruck O., Michel R., Rösel R., Meltzow B., Schiekel T., Sudbrock F., Herpers U., Filges d., Bonani G., Dittrich-Hannen B., Suter M., Kubik P. W., and Synal H.-A. 2000b. Simulation of the interaction of galactic cosmic-ray protons with meteoroids: On the production of radionuclides in thick gabbro and iron targets irradiated isotropically with 1.6 GeV protons. *Meteoritics & Planetary Science* 35:287–318.

Leya I., Neumann S., Wieler R., and Michel R. 2001a. The production of cosmogenic nuclides by galactic cosmic-ray particles for 2ð exposure geometries. *Meteoritics & Planetary Science* 36:1547–1561.

Leya I., Graf Th., Nishiizumi K., and Wieler R. 2001b. Cosmic-ray production rates of helium, neon, and argon isotopes in H chondrites based on chlorine-36/argon-36 ages. *Meteoritics & Planetary Science* 36:963–973.

Leya I., Begemann F., Weber H. W., Wieler R., and Michel R. 2004a. Simulation of the interaction of galactic cosmic ray protons with meteoroids: On the production of ^{3}H and light noble gas isotopes in isotropically irradiated thick gabbro and iron targets. *Meteoritics & Planetary Science* 36:367–386.

Leya I., Gilabert E., Lavielle B., Wiechert U., and Wieler R. 2004b. Production rates for cosmogenic krypton and argon isotopes in H chondrites with known ^{36}Cl-^{36}Ar ages. *Antarctic Meteorite Research* 17:185–199.

Leya I., Ammon K., Lavielle B., Gilabert E., Wieler R., David J.-C., and Michel R. 2008. Production of noble gas isotopes by proton-induced reactions on Mg, Al, Si, Fe, Ni, Pb, and Bi. *Proceedings of the International Conference on Nuclear Data for Science and Technology.* pp. 1061–1064.

Lipschutz M. E., Signer P., and Anders E. 1965. Cosmic ray exposure ages of iron meteorites by the ^{21}Ne/^{26}Al method. *Journal of Geophysical Research* 70:1473–1489.

Lüpke M. 1993. Untersuchung zur Wechselwirkung galaktischer Protonen mit Meteoroiden—Dicktarget Simulationsexperimente und Messung von Dünntarget-Wirkungsquerschnitten. PhD. Thesis, University Hannover, Gemany, 260 p.

Masarik J. and Reedy R. C. 1994. Effects of bulk composition on nuclide production processes in meteorites. *Geochimica et Cosmochimica Acta* 58:5307–5317.

Mason B. 1979. Cosmochemistry Part 1. Meteorites. In *Data of geochemistry*, edited by Fleischer F. Geological Survey Professional Paper 440-B-1. pp. B1–B132.

Michel R., Dragovitsch P., Englert P., Peiffer F., Stück R., Theis S., Begemann F., Weber H., Signer P., and Wieler R., Filgesand D., Cloth P. 1985. On the depth-dependence of spallation reactions in a spherical thick diorite target homogeneously irradiated by 600 MeV protons. Simulation of production of cosmogenic nuclides in small meteorites. *Nuclear Instruments and Methods in Physics Research B* 16:61–82.

Michel R., PeifferF., Theis S., Begemann F., Weber H., Signer P., Wieler R., Cloth P., Dragovitsch P., Filges D., Englert P. 1989. Production of stable and radioactive nuclides in thick stony targets (R = 15 and 25 cm) isotropically irradiated with 600 MeV protons and simulation of the production of cosmogenic nuclides in meteorites. *Nuclear Instruments and Methods in Physics Research B* 42:76–100.

Michel R., Dragovitsch P., Cloth P., Dagge G., and Filges D. 1991. On the production of cosmogenic nuclides in meteoroids by galactic protons. *Meteoritics* 26:221–242.

Michel R., Lüpke M., Herpers U., Rösel R., Filges D., Dragovitsch P., Wölfli W., Dittrich B., and Hofmann H. J. 1993. Simulation of the interactions of galactic cosmic ray protons by irradiation of a thick stony target with 1.6 GeV protons. *Journal of Radioanalytical and Nuclear Chemistry* 169:13–25.

Nagai H., Honda M., Imamura M., and Kobayashi K. 1993. Cosmogenic ^{10}Be and ^{26}Al in metal, carbon, and silicate of meteorites. *Geochimica et Cosmochimica Acta* 57:3705–3723.

Nakamura T., Sugita H., Imamura M., Uwamino Y., Nagai H., and Kobayashi K. 1991. Measurement of the long-lived ^{26}Al production cross section in the ^{27}Al(n,2n) reaction. *Physical Review C* 43:1831–1837.

Nakamura T., Sugita H., Imamura M., Uwamino Y., Shibata S., Nagai H., Tabanatake M., and Kobayashi K. 1992. Measurement of long lived ^{10}Be, ^{14}C and ^{26}Al production cross sections for 10–40 MeV neutrons by accelerator mass spectrometry. In *Proceedings of the International Conference on Nuclear Data for Science and Technology.* pp. 714–716.

Nishiizumi K., Regnier S., and Marti K. 1980. Cosmic ray exposure ages of chondrites, pre-irradiation and constancy of cosmic ray flux in the past. *Earth and Planetary Science Letters* 50:156–170.

Nishiizumi K., Elmore D., Honda M., Arnold J. R., and Gove H. E. 1983. Measurements of ^{129}I in meteorites and lunar rocks by tandem accelerator mass spectrometry. *Nature* 305:611–612.

Nishiizumi K., Kubik P. W., Elmore D., Reedy R. C., and Arnold J. R. 1989. Cosmogenic 36Cl production rates in meteorites and the lunar surface (abstract). 19th Lunar and Planetary Science Conference. pp. 305–312.

Nyquist L., Funk H., Schultz L., and Signer P. 1973. Spallogenic rare gases in the El Taco meteorite. *Earth and Planetary Science Letters* 2:241–248.

Palme H. and Jones A. 2003. Solar system abundances of elements, pp. 41–61. In *Meteorites, comets, and planets*, edited by Davis A. M. Treatise on Geochemistry, vol. 1. Oxford: Elesevier.

Pearlstein S. 1987. Systematics of neutron emission spectra from high-energy proton bombardement. *Nuclear Science Engineering* 95:116–127.

Reedy R. C. and Arnold J. R. 1972. Interaction of solar and galactic cosmic ray particles with the Moon. *Journal of Geophysical Research* 77:537–555.

Reedy R. C., Herzog G. F., and Jessberger E. K. 1979. The reaction Mg(n,alpha)Ne at 14.1 MeV and 14.7 MeV: Cross sections and implications for meteorites. *Earth and Planetary Science Letters* 44:341–348.

Reedy R. C., Masarik J., Nishiizumi K., Arnold J. R., Finkel R. C., Caffee M. W., Southon J., Jull T. A. J., and Donahue D. J. 1993. Cosmogenic-radionuclide profiles in Knyahinya: New measurements and models (abstract). 24th Lunar and Planetary Science Conference. pp. 1195–1196.

Sarafin R. 1985. Anwendung radiochemischer Methoden und der Beschleuniger-Massenspektrometrie zur Bestimmung der tiefenabhängigen, langlebigen Spallations-Radionuklide ^{10}Be, ^{26}Al, ^{36}Cl und ^{53}Mn in Steinmeteoriten und Gedanken zum noch ungeklärten Ursprung der Shergotitte. Ph.D. University of Cologne, Germany.

Schnabel C., Gartenmann P., Lopez-Gutiérrez J. M., Dittrich-

Hannen B., Suter M., Synal H.-A., Leya I., Gloris M., Michel R., Sudbrock F., and Herpers U. 1998. Determination of proton-induced production cross sections and production rates of ^{129}I and ^{41}Ca. In *Proceedings of the International Conference on Nuclear Data for Science and Technology.* pp. 1559–1561.

Schnabel C., Leya I., Michel R., Csikai J., Dezso Z., Lopez-Gutierrez J. M., and Synal H.-A. 2000. Non-destructive and radiochemical determination of the neutron-induced production cross section of I-129 from Te and other neutron-induced cross sections on Te at 14.7 MeV. *Radiochimica Acta* 88:439–443.

Schnabel C., Leya I., Gloris M., Michel R., Lopez-Gutiérrez J. M., Krähenbühl U., Herpers U., Kuhnhenn J., and Synal H.-A. 2004. Production rates and proton-induced production cross sections of ^{129}I from Te and Ba: An attempt to model ^{129}I production in stony meteoroids and ^{129}I in a Knyahinya sample. *Meteoritics & Planetary Science* 39:453–466.

Schultz L. and Hintenberger H. 1967. Edelgasmessungen an Eisenmeteoriten. *Zeitschrift für Naturforschung Teil A* 22:773–779.

Schultz L. and Signer P. 1976. Depth dependence of spallogenic helium, neon, and argon in the St. Severin chondrite. *Earth and Planetary Science Letters* 30:191–199.

Shubin Y. N., Lunev V. P., Konobeyev A. Y., Dityuk A. I. 1995. Computer code ALICE-IPPE, *IAEA INDC(CCP)-385*, Vienna, Austria.

Signer P. and Nier A. O. 1960. The distribution of cosmic-ray produced rare gases in iron meteorites. *Journal of Geophysical Research* 65:323–381.

Signer P. and Nier A. O. 1962. The measurement and interpretation of rare gas concentrations in iron meteorites. In *Research on meteorites*, edited by Moore C. B. New York: Wiley. pp. 7–35.

Stauffer H. 1962. On the production ratios of rare gas isotopes in stone meteorites. *Journal of Geophysical Research* 67:2023–2028.

Vogt S. 1988. Untersuchungen zur tiefenabhängigen Produktion langlebiger kosmogener Nuklide in Meteoriten. Ph.D. thesis, Universität zu Köln, Germany, 150 p.

Wasson J. T. and Kallemeyn G. W. 1988. Composition of chondrites. *Philosophical Transactions of the Royal Society of London A* 325:535–544.

Welten K. C., Caffee M. W., Leya I., Masarik J., Nishiizumi K., and Wieler R. 2003. Noble gases and cosmogenic radionuclides in the Gold Basin L4 chondrite shower: Thermal history, exposure history, and pre-atmospheric size. *Meteoritics & Planetary Science* 38:157–173.

Wieler R. 2002. Cosmic-ray-produced noble gases in meteorites. In *Noble gases*, edited by Porcelli D. P., Ballentine C. J., and Wieler R. Reviews in Mineralogy and Geochemistry, vol. 47. Washington, D.C.: Mineralogical Society of America. pp. 125–170.